Biomedical Engineer master's degree
Department of Mechanical and Aerospace Engineering
Politecnico di Torino, Turin, Italy

Approximating near-wall mass transport in human arteries with wall shear stress topological skeleton analysis

Giulia Ingrami Bianchini
******

Supervisor:

Prof. Umberto Morbiducci, Supervisor
Giuseppe De Nisco, Co-supervisor
Diego Gallo, Co-supervisor

Examination Committee:

De Nisco Giuseppe, Politecnico di Torino
Gallo Diego, Politecnico di Torino
Manuello Bertetto Andrea, Politecnico di Torino
Marcolin Federica, Politecnico di Torino
Morbiducci Umberto, Politecnico di Torino
Terzini Mara, Politecnico di Torino

Politecnico di Torino 2020/2021

Abstract

Atherosclerosis, representing the main cause of death in Western World, is a complex, multifactorial, arterial disease, influenced by local biological, biomechanical, and systemic factors. Among biomechanical factors, local hemodynamics plays a major role in promoting the initiation/progression of atherosclerotic disease in human arteries. In detail, the exposure to low and oscillatory wall shear stress (WSS) phenotype is widely recognized as marker of deranged hemodynamics, leading to atherosclerosis onset and progression. Only recently, evidence of the moderately weak ability of low/oscillatory WSS to predict plaque localization and endothelial disfunction at the early stage underlined that currently considered hemodynamic features may oversimplify the complexity to which the arterial luminal surface is exposed. In this contest a marked interest recently emerged on the topological skeleton of the WSS vector field. The WSS topological skeleton consists in: (a) WSS fixed points, focal points where the WSS vector vanishes, and (b) WSS manifolds, identifying the WSS contraction/expansion regions at the luminal surface, linking fixed points. WSS

topological skeleton features allow the identification of flow features like flow stagnation, recirculation and separation which are classified as “aggravating” biomechanical events, linked to “aggravating” biological events. Among the aggravating biological events for atherosclerosis onset/progression, mass transport processes are markedly involved by mediating, e.g., the accumulation of lipids at the arterial wall. Mass transport mechanism, are, in turn, influenced by local hemodynamics, which may promote, e.g., low-density lipoproteins (LDL) and monocyte receptor expression on the endothelium. These mechanisms are causally related to the development of the disease. For this reason, Lagrangian-based features of WSS topological skeleton has been suggested to provide a template of near-wall mass transport. However, the complexity of the Lagrangian-based method requires high computational costs. To overcome this limitation, a Eulerian method to analyse WSS topological skeleton has been recently proposed by Mazzi and co-workes. In this contest, the aim of this work was to test the ability of the recently proposed Eulerian-based features of WSS topological skeleton to provide a template of blood-to-wall LDL transfer, in patient-

specific computational models of human arteries. do that, starting from medical images of one arterial segment per ostensibly healthy subject involved in the study, the lumen geometry of the carotid bifurcation and the right coronary artery (RCA) were reconstructed. For each geometry, high-quality mesh was built into the ICEM environment, with a focus on the near-wall region, modelized by 30 layers of high-quality prismatic cells to properly simulate the blood-to-wall LDL transfer. The finite volume method was applied to solve the discretized form of the Navier-Stokes equations coupled with a discretized form of advection-diffusion equations. A constant value of LDL concentration C0 (equal to the LDL mean concentration in the whole blood) was applied at the inlet section, and the stress-free condition was set at the outlets. A proper equation was used to model the LDL transfer at the wall. As for fluid motion, measured flow rates were prescribed as inflow condition for each model, in terms of flat velocity profile. At the outlets of each model, measured flow rates were imposed as flow ratio or mass flux. A uniform LDL concentration equal to C0 was applied in the whole domain.

Near-wall hemodynamics was analysed in terms of (a) classical WSS-based descriptors (i.e., TAWSS, OSI, RRT) and (b) WSS topological skeleton. In detail, WSS manifolds were identified by the divergence of the normalized WSS vector field (negative values of normalized WSS divergence identify WSS contraction regions, while positive values identify WSS expansion regions); WSS fixed points were identified by the Poincaré index and classified based on the eigenvalues of the Jacobian matrix. Finally, luminal surface exposed to deranged hemodynamics, cycle-average WSS contraction regions and local LDL uptake where identified by computing objective thresholds, as the lower 10th percentile for TAWSS and cycle-average normalized WSS divergence (DIV), upper (90th) for OSI, RRT and LDL luminal concentration. These areas were named as TAWSS10, DIV10, OSI90, RRT90 and LDL90, respectively. The ability of each hemodynamic descriptor to identify local LDL uptake was assessed in terms of Similarity Index (SI), quantifying the overlap of each one among TAWSS10, DIV10, OSI90 and RRT90, with LDL90. Results from this study highlighted a marked co-localization between cycle-average WSS contraction regions and LDL polarization at the luminal surface of each investigated model. WSS

contraction action and LDL polarization mainly occurred at the basis of carotid bifurcation and along the inner curvature wall of the right coronary artery. The similarity analysis confirmed these qualitative observations: DIV10 markedly co-localized with LDL90, with higher SI with respect to classical WSS descriptors (from 60% to 85% higher). In conclusion, findings from this work indicate that: (a) the recently proposed Eulerian-based WSS topological skeleton features provide an effective template of the LDL blood-to-wall transfer, reducing computational costs of classical techniques; (b) WSS contraction regions at the luminal surface co-localize with LDL luminal polarization (better than classical WSS-based descriptors of deranged hemodynamics). The latter suggest that the contraction action exerted by WSS at the endothelium may promote near-wall mass transfer and that WSS contraction regions can be used as surrogate marker of near-wall mass transfer. All these evidences stimulate further investigation on the effects of WSS topological skeleton on vascular pathophysiology, suggesting its contribution to a deeper understanding of the hemodynamics-driven processes.

Acknowledgments

At the end of this of this journey I wish to give special thanks to some important people.

First of all, to all my family which was near to me despite the hard time and the distance.

To my mother, always there to listen and advise me in every aspect of my life.

To my father, I hope I made you proud.

To my aunt and her amazing and strong way to face difficulties which inspire me since I can remember and to my grandmother with all my affection and love.

A special thank goes to Francesca who bears me and stand beside me from the beginning of this journey and without which my life would have had less colourful shades.

I would like to thank my supervisor Giuseppe De Nisco who, despite the hard time and hard communication methods, was able to teach me and immerge me in the subject; thank you for your patience.

At the end I wish to thank also all my friends and colleagues who made this adventure a little “spicier” with their presence and support.

Chapter 1

Introduction

1.1 Anatomy of cardiovascular district

1.1.1 The cardiovascular system

The cardiovascular system provides oxygen and nutrients to the whole body, regulates temperature and pH and maintains homeostasis. It consists of three main structures: the *heart*, the *blood* and the *blood vessels*. The *heart* represents an anatomical pump that generates the appropriate pressure to make blood reach all the organs and

systems requiring oxygen. It is divided into four chambers: two atrium and two ventricles, both right and left.

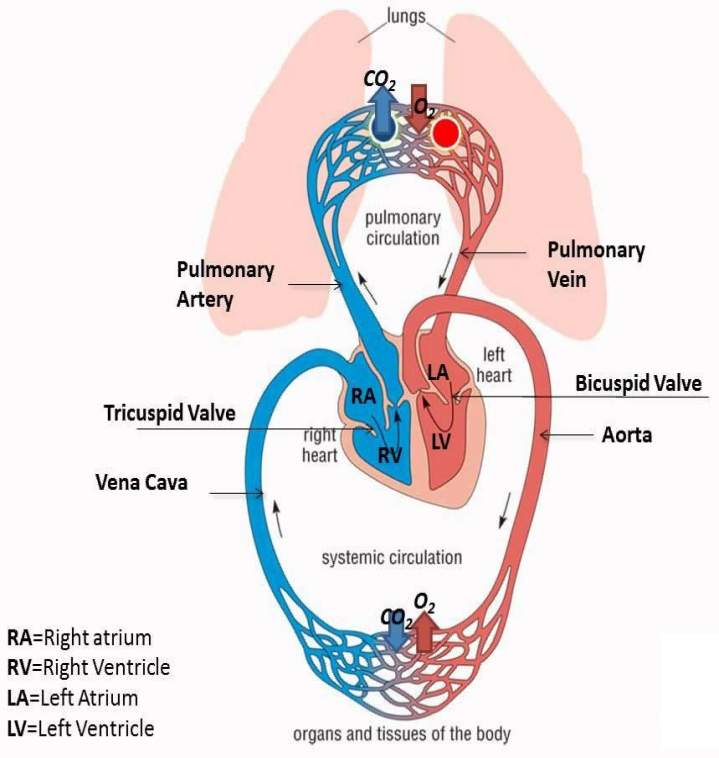

Figure 1.1 A sketch of the cardiovascular system underlining the pulmonary and systemic circulations (from www.socratic.org).

Two different circulation loops originate from the heart: the *pulmonary* and the *systemic circulation* (*figure 1.1*). Each circulation loop is controlled by a specific part of the heart (left and right). The pulmonary circulation oxygenates de-oxygenated blood: it starts from the right ventricle, leads the

blood through the lungs and goes back to the left atrium. From the left atrium, oxygenated blood reaches the left ventricle to be pumped through the systemic circulation to the organs. Through the venous return, de-oxygenate blood, full of carbon dioxide, is sent back to the right atrium, completing the systemic circulation loop. *Blood* is a biological fluid delivering oxygen and nutrients to the body organs and cells and transporting metabolic waste away from them. It is composed by blood cells suspended in a plasma solution. The blood cells are *erythrocytes* (red blood cells), *leucocytes* (white blood cells) and *platelets*. The red blood cells are small cells with an average diameter of 8-9 micrometres, a density of 1.098 g/cm^3 (Schneck et al., 1995) and no nucleus. The presence of haemoglobin in the erythrocyte's cytoplasm allows red blood cells to bond oxygen irreversibly. The white blood cells, as part of the immune system, protect the body against infectious disease. They are caractherized by a density of about 1.055 to 1.085 g/cm^3 and a diameter of 6 to 10 micrometres. Platelets, with a diameter of 3 micrometres and a density of 1.085 g/cm^3, provide the maintaining of homeostasis. The blood plasma is a fluid mostly composed by

water which contains important proteins (like albumins, globulins and fibrinogen), hormones, oxygen and carbon dioxide. Blood is carried through the body by an efficient and organized link of *blood vessels* with different dimensions and functionality: the *arteries*, made up by smooth muscles, collagen and elastin in order to sustain the high pressure stress applied by the heart, gentle decrease their dimension going through peripheral areas becoming *arterioles* and *capillaries*. The *capillaries* go on merging into *venules* which merge into *veins*. *Veins* are smaller than *arteries* and provides the venous return to the heart through small valves located into the vessel lumen. *Veins* are also more rigid than arteries due to the lower pressure stress to which they are subjected. The arteries are made up by three different concentric layers: tunica *intima*, *media* and *adventitia*. The tunica intima is the inner layer and his antithrombogenic surface allows transfer of macromolecules through the other layers. Inside the vessels a hollow area, the lumen, allows the flowing of the bloodstream. Vessel's histology and organic responses are well analysed in the following paragraph.

1.1.2 Histology of blood vessels

Bloodstream is pumped through a complex vessel network by the action of the heart. Two distinct phases are responsible for the blood flow over the body: *systole* and *diastole*. During the *systole* the blood is pumped out of the heart and it rests in the heart during the *diastole*, while the heart itself is being filled with the oxygenated blood coming from the pulmonary circulation. As previously stated, the network responsible for the bloodstream is made up by arteries and veins. Arteries walls are arranged into three different concentric layers called tunica *intima*, *media* and *adventitia*. The inner layer is the *tunica intima* and it is composed by a single layer of endothelial cells and a small amount of connective tissue. The endothelial cells are the only barriers between the blood flow and the vessel wall, and they provide an antithrombogenic surface, essential to avoid thrombus formation and regulate the blood-to-wall transfer of proteins and nutrients. The *intima* is separated from the *tunica media* by an elastic membrane called *internal elastic lamina* which is a discontinuous layer allowing some muscle cells to penetrate the tunica. The *tunica media* is

predominantly composed by smooth muscle cells, connective tissue and elastic fibres. It is the thickest layer of the vessel wall and his composition provides the vessel with the elasticity and compliance needed to adapt itself during the cardiac cycle, by accumulating and releasing energy given by the pressure variations. The *media* is separated from the *tunica adventitia* by a dense elastic membrane called the *external elastic lamina*. The *adventitia* is mainly composed by collagen and elastic fibres that allow the vessel the anchoring to the nearby organs to properly transfer nutrients and oxygen and to protect the vessel in case of large deformations by preventing the vessel's cloth.

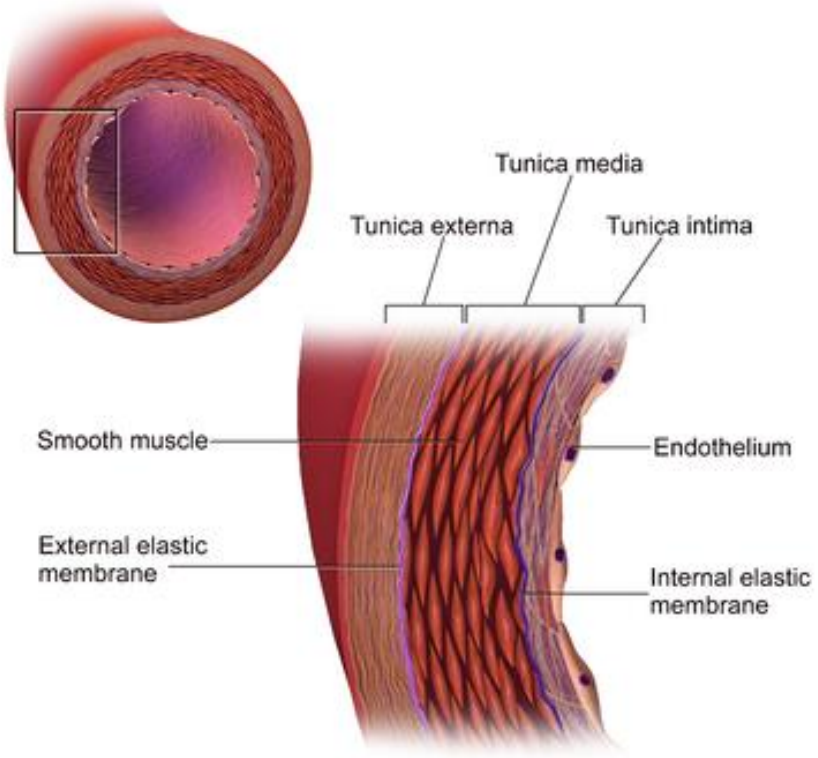

Figure 1.2 A schematic representation of the three concentric layers composing the vessel wall. *Tunica intima*, *media* and *adventitia* are separated by two different membrane: internal elastic *lamina* and external elastic *lamina* (image from www.techpe.com).

Close to the organs, arteries are characterized by a very small size and are named as *capillaries*. Their wall consists of a single layer of endothelial cells laying on a membrane. For all these reasons, arteries are considered dynamic structures that follow the bloodstream and rearrange themselves according to the flow. This ability is necessary to make the

vessel follow the pressure variations of the cardiac cycle, but it may also lead to critical conformational changes which are strongly linked to the insurgence of cardiovascular diseases.

1.1.3 Carotid Bifurcation and Right Coronary Artery

The attention of this project was focused on two main cardiovascular districts: the *carotid bifurcation* and the *right coronary artery* (RCA).

The carotid bifurcation is located at the distal part of the *common carotid artery* (CCA), where the *internal carotid artery* (ICA) and *external carotid artery* (ECA) originate. In detail, the CCA rises from the neck of the brachiocephalic artery (if right CCA) or from the aortic arch (if left CCA) to the cerebral circulation. At the level of the fourth cervical vertebra the CCA bifurcates into the ICA, which supplies blood to the brain, and the ECA, supplying blood to the neck and the face. Moreover, the carotid sinus, situated at the bottom of the ICA in the carotid bifurcation, contains sensors that helps regulate the blood pressure. Due to his anatomical

features and geometry, the carotid bifurcation is one of the preferential districts that leads to the genesis of atherosclerotic plaques.

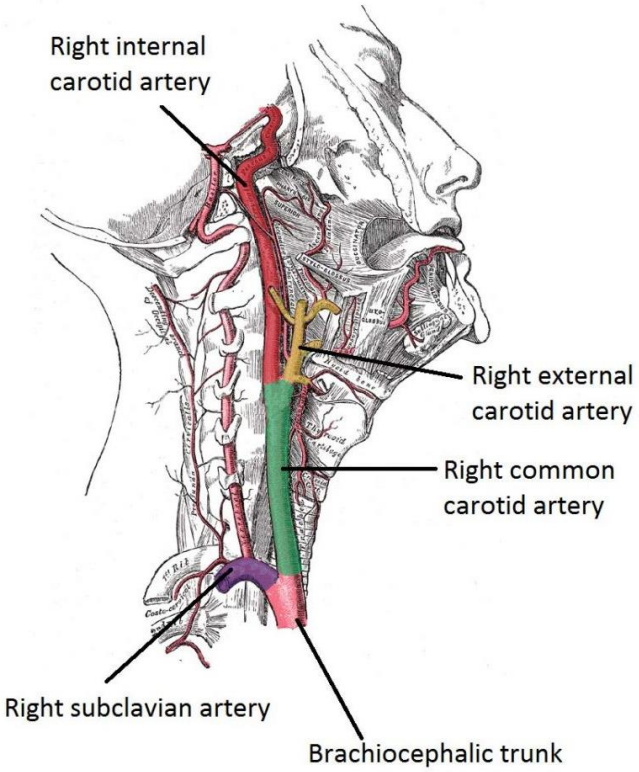

Figure 1.3 A sketch of the human right carotid artery. Different colours were used to define the internal carotid artery (red), the external carotid artery (yellow) and the common carotid artery (green) (www.TeachMeAnatomy.com).

The *right coronary artery* (RCA) is part of the coronary circulation which supplies blood to the myocardium. It originates from the right aortic sinus of the ascending aorta and runs down wrapping around the right side of the heart. It branches into the posterior descending artery and the right marginal artery. The RCA gives rise to several secondary arteries which supply blood to the right part of the heart and part of the blood to the left ventricle.

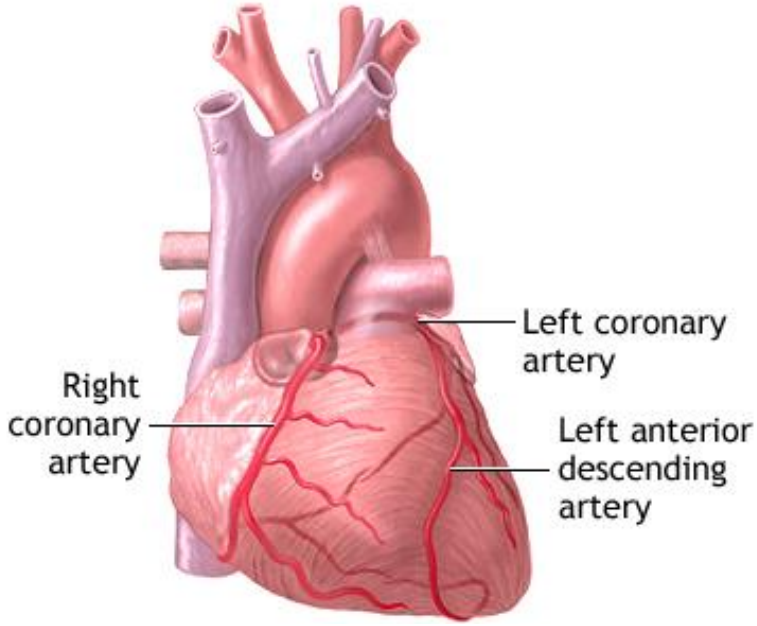

1.4 A representation of the human coronary circulation with a focus on the right coronary artery, the left coronary artery and the left anterior descending artery (*from adam.com*).

1.2 Atherosclerosis

Atherosclerosis is a specific form of a cardiac disease consisting in the gradual thickening and hardening of the vessel, which leads to a narrowing of the vessel's lumen. The consequence is a lower blood supply to some specific districts and a higher effort required from the heart. The worst consequences of atherosclerosis are heart stroke and ictus, which are the main cause of death in the Western World. The progression of this cardiovascular disease is very slow, it can begin during childhood and never become a problem for the patient. However, if the trigger factors are favourable and combine themselves in unknow ways, the atheromatic plaques may undergoes to the complete lesion which causes clinical evidences of the pathology (critical stage of the disease).

1.2.1 Epidemiology

There is ample evidence that the genesis of atherosclerosis is linked to different systemic factors, such as obesity, cigarettes smoke, diabetes, stress and genetic factors (Patel

et al., 1980). This progressive disease starts with the genesis of few plaques in different districts of the arterial lumen surface. This is the first step of atherogenesis, the developmental process of atheromatic plaques. One hypothesis suggests that leukocytes, such as monocytes or basophils, begin to attack the endothelium of the artery lumen in cardiac muscle. The consequent inflammation leads to the generis of the atheromatic plaques in the tunica intima. Early atherogenesis is characterized by the adherence of monocytes (white blood cells) to the vascular bed lining, the endothelium, then by their migration to the sub-endothelial space, and further activation into monocyte-derived macrophages (Swirski et al., 2013) . The primary documented driver of this process are oxidized lipoprotein particles within the wall. Low-density lipoprotein (LDL) particles in blood plasma invade the endothelium and are oxidized by a set of biochemical reactions, involving enzymes and free radicals in the endothelium. Oxidized LDL releases toxins which cause the recruiting of more monocytes from the blood flow. This increase wall injury allowing more LDL to penetrate the arterial wall. The monocytes who turn into

macrophages, ingest oxidized LDL leading to the growth of lipid foam cells (cells with a high lipid content due to numerous cytoplasmatic vesicles), the early stage of the atheromatic plaque. Within some years the number of plaques and the plaques themselves are going to grow, protrude inside the vessel lumen and compromise the physiological blood flow. The atheromatic plaque can also ulcerate, leading to the genesis of a thrombus that clog the blood vessel completely.

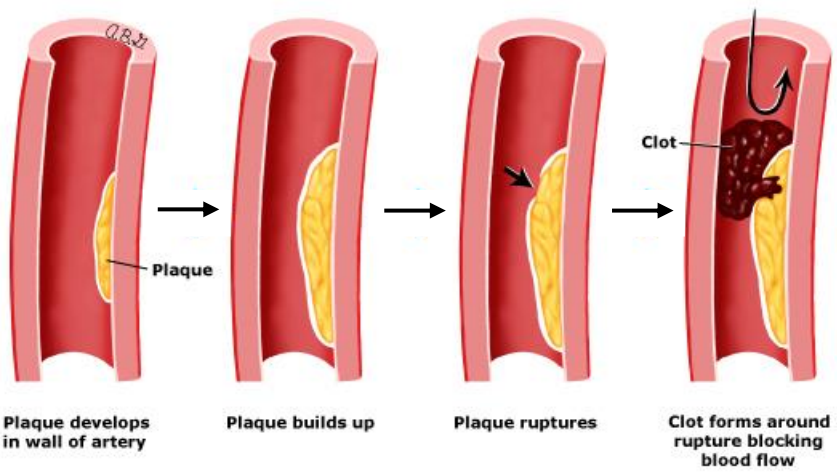

Figure 1.5 A sketch of human vessel representing the progression of an atheromatic plaque which leads to a narrowing of the vessel's lumen. The last step of the disease is the rupturing of the plaque which cause a thrombus formation in the vessel (*image from uptodate.com*).

1.2.2 Low-density Lipoproteins

Low-density lipoproteins are the most abundant group of lipoproteins which transport fat around the body through extracellular water. There are five groups of lipoproteins: *ultra-low density lipoproteins* (ULDL), *very low-density lipoproteins* (VLDL), *intermediate-density lipoproteins* (IDL), *low-density lipoproteins* (LDL) and *high-density lipoproteins* (HDL). A single LDL particle is about 22 nanometres in diameter, and it transport from about 3000 to 6000 fat molecules per particle. Each particle contains a single apolipoprotein B-100 molecule (Apo B-100) and also from 80 to 100 additional ancillary proteins. Each LDL particle has a highly hydrophobic core made up by polyunsaturated fatty acid and from hundreds to thousands (about 1500) esterified and unesterified cholesterol molecules. The core also hosts triglycerides and other fats and is surrounded by a shell of phospholipids and unesterified cholesterol, as well as the single copy of Apo B-100. When cell requires cholesterol, LDL receptor are synthetized and inserted into the plasma membrane. LDL receptors bound with LDL are delivered, through vesicles, to the endosome characterized by a low pH

level. Because of the low pH, LDL receptors undergoes a conformational change and release LDL. Once the correct amount of cholesterol has been delivered, the cell itself stops to generate LDL receptors to interrupt this cycle preventing an overabundance of cholesterol. It has been proved that oxidized LDL within wall arteries is one of the major causes that leads to atherogenesis and it may be caused by several mechanisms. First, LDL receptors are not able to recognize the LDL due to his conformational change caused by oxidation. The non-recognition triggers the recruitment of monocytes and activate an inflammatory process which leads to the growth of an atheromatic plaque (Stocker at al., 2004). Glycation is another type of atherogenic modification of LDL that may contribute to atherosclerosis (Amir et al., 2000). Glycation is the covalent bond of a sugar to a protein or lipid without an enzyme. Small and dense molecules of LDL appear to be susceptible to glycation which has been proved to be strongly linked to LDL oxidation. Moreover, products of oxidized LDL may induce vascular wall cells to produce cytokines which promote recruitment of inflammatory cells into the vascular wall, increasing the inflammatory process.

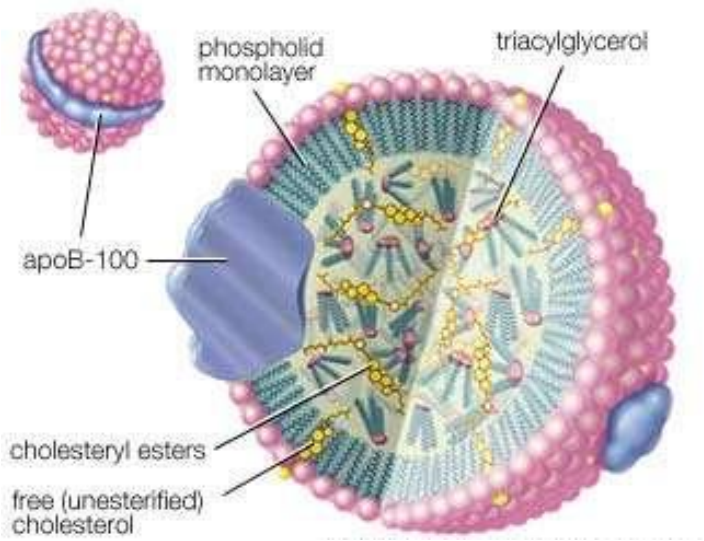

Figure 1.6 A representation of a low-density lipoprotein formed by an external membrane made up by a phospholid monolayer and encircled by a single apoB-100 molecule (*image from Britannica.com*).

1.2.3 Hemodynamic in Atherosclerosis

Previous evidences (e.g. Stocker et al., 2008) underline that, beside systemic or biological risk factors, atherosclerosis onset and progression is also linked to peculiar hemodynamic features developing into the vessel lumen. Indeed, atheromatic plaques mostly develop at bifurcations, bends and branches of the arterial tree, districts where the physiological blood flow may be “disturbed” by the

establishment of flow conditions as blood recirculation, stasis and flow separation and reattachment to the wall, usually classified as "*disturbed flow*" events, which may promote the initiation and progression of the atherosclerotic disease (Stocker et al., 2008).

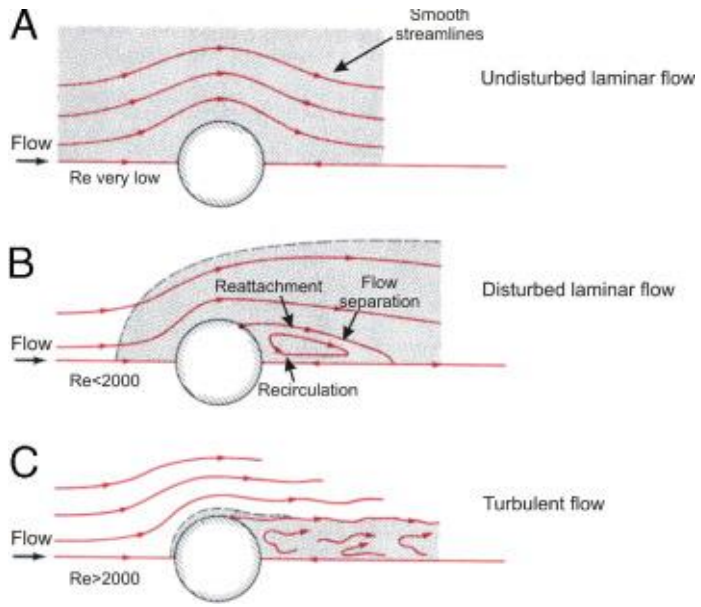

Figure 1.7 A sketch of different types of flows displayed by straight (A), curved (B) and non-regular streamlines (C) (*image from sciencedirect.com*).

To identify luminal regions exposed to unfavourable hemodynamic conditions, several descriptors have been suggested, mainly based on the *wall shear stress* (WSS) (Pinto

et al., 2016). The WSS is considered the “footprint” of the blood flow on the vessel’s wall and it expresses the force per unit area exerted by the blood flow at the endothelium in a direction on the local tangent plane. Physiological hemodynamic conditions are characterized by physiological high values of WSS, while districts exposed to “disturbed flow” are characterized by low and oscillatory WSS values. For this reasons, hemodynamics can be described by the following “well established” descriptors: *time-averaged wall shear stress* (TAWSS), used to highlights low WSS magnitude districts over the cardiac cycle, *oscillatory shear index* (OSI), which underlines zone where WSS vectors over-oscillates and *relative residence time* (RRT), which summarize information from the previous descriptors (Pinto et al., 2016).

1.2.3.1 WSS topological skeleton

WSS-based descriptors, used to identify low and oscillatory wall shear stress regions, were proved to be significant but weak predictors of lesion localization (Peiffer et al., 2013).

Indeed, the commonly used hemodynamic descriptors, based only on WSS magnitude or direction, may oversimplify the complex hemodynamics to which the luminal surface is exposed. For this reason, a high interest recently emerged on the topological skeleton of WSS vector field (Mazzi et al., 2020, De Nisco et al., 2020, Morbiducci et al, 2020). The WSS topological skeleton consists of: WSS fixed points (Figure 1.9B), which are luminal points were the WSS vector vanishes (thus indicating low WSS focal luminal regions), and stable/unstable WSS manifolds (Figure 1.9A), connecting fixed points and highlighting the expansion/contraction action exerted by WSS vector at the luminal surface.

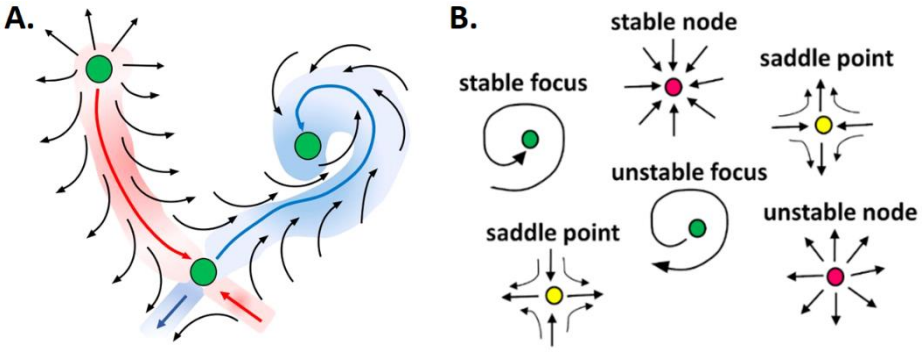

Figure 1.8 A. Sketch of the WSS manifolds: contraction regions (blue) and expansion regions (red); **B.** Classification of WSS fixed points: stable/unstable nodes, stable/unstable focus and saddle points are depicted.

WSS topological skeleton is instrumental in quantifying the complex and dynamic features of the WSS vector field and is strongly linked with characteristic flow features classified as "*disturbed flow*" events (i.e. flow stagnation, separation and recirculation regions). Here, the recently proposed Eulerian-based approach (Mazzi et al., 2020) was used to analyse WSS topological skeleton through manifold and fixed points.

1.2.4 Mass transport in Atherosclerosis

Local hemodynamics influences also mass transport, which is, in turn, involved in atherosclerotic diseases onset/development. As analysed by Tarbell et al. in 2003, mass transport is responsible for mediating the focal accumulation of lipid in arteries through the modulation of fluid mechanical forces. There are four mass transport mechanisms that are considered important in the localization of atherogenesis: *blood phase-controlled hypoxia*, *leaky endothelial junctions, transient intracellular junction remodelling* and *convective clearance of the subendothelial intima and media* (Tarbell et al, 2003). In detail, each solute

transported from the bulk to the endothelial surface will be submitted to different boundary conditions, depending on the molecule being transported (e.g. if the molecule is soluble, submitted to enzyme-catalysed reactions or solubilized in vesicles). The first mechanism is based on hypoxia. Oxygen may be fluid-phase limited in region of low fluid-phase mass transfer rates such as outer walls of bifurcations and inner walls of curved regions. The leak of oxygen is likely to induce atherogenesis for different reasons: hypoxia induces cells apoptosis which can increase LDL transport through “leaky junctions” (junctions with a dimensions of 30-1000 nm, which occupy a small fraction of the surface area) and besides, an endothelial break down of the barriers may occur, increasing macromolecular transport by forming inter-endothelial gaps. The second mechanism highlight the role of the previously named “leaky junctions” in the transport of macromolecules across the endothelial layer. As for the third mechanism, it underlines the strong link between hemodynamics changes in blood flow and the response of mass transport pathways to these changes. Intracellular junctions (tight and adherents junctions), for

instance, tends to remodel themselves affecting endothelial transport of LDL molecules. The fourth mechanism focus the attention on large macromolecules, such as LDL, with a low endothelial permeability (P_e) relative to the volume flux (J_v). These molecules are more likely to accumulate in presence of factors that reduce J_v without altering P_e. One of these factors, as demonstrated by Lever at al. in 1996, could be the presence of a collar around arteries which increase steady state levels of LDL in the tunica media of the vessels. Among the described mechanisms, hemodynamics plays a fundamental role both in terms of "*passive*" and "*active*" transport (Malek et al., 1999). *Passive transport* (i.e. advection and diffusion) is based on the movement of molecules down a gradient while *active transport* uses cellular energy to move them against gradient and it appears to promote LDL and monocyte receptor expression on endothelial cells.

1.2.5 Consequence of Atherosclerosis

As previously stated, atherosclerosis starts with the formation of atheromatic plaques made up by fat molecules.

This leads to a narrowing and hardening of some vessel's districts which alters the blood flow and the amount of blood destinated to body districts. Consequences of this disease depend on the district of the body affected and on the type of plaques formed on the vessel's wall. As the disease is progressive, the formation of the atheromatic plaque is a very slow process and the vessel can adapt and remodel itself in order to maintain the correct blood flow. This conformational change is a body weapon to survive to the slow progression of the disease. When the lumen occlusion is to wide (over 70% of the lumen is occupied by the plaque), the patient is going to suffer from clinical complication as heart failure. Otherwise, a rupture of the atheromatic plaque may occur. In this situation the extracellular matrix of the lesion breaks, and the exposed thrombogenic components of the plaque, mainly collagen, will trigger a thrombus formation. This leads to a quick occlusion of the lumen which damage distal tissues as a result of inadequate blood flow. If the thrombus formation occurs in an artery of the brain circulation (e.g. carotid artery) it may lead to a stoke.

Otherwise, if the cardiac circulation is affected (e.g. coronary artery), the blood clotting may cause a myocardial infarction.

1.3 Motivation and aim of the thesis

Atherosclerosis, representing the main cause of death in Western World, is a complex, multifactorial, arterial disease, influenced by local biological, biomechanical, and systemic factors (Kwak et al., 2014, Morbiducci et al, 2016). Among biomechanical factors, local hemodynamics plays a major role in promoting the initiation/progression of atherosclerotic disease in human arteries. In detail, the exposure to low and oscillatory wall shear stress (WSS) phenotype is widely recognized as marker of deranged hemodynamics, leading to atherosclerosis onset and progression (Malek et al., 1999). Only recently, evidence of the moderately weak ability of low/oscillatory WSS to predict plaque localization and endothelial disfunction at the early stage underlined that currently considered hemodynamic features may oversimplify the complexity to which the arterial luminal surface is exposed (Peiffer et al., 2013). In this

contest a marked interest recently emerged on the topological skeleton of the WSS vector field (Mazzi et al., 2020, De Nisco et al., 2020, Morbiducci et al, 2020). The WSS topological skeleton consists in: (a) WSS fixed points, focal points where the WSS vector vanishes, and (b) WSS manifolds, identifying the WSS contraction/expansion regions at the luminal surface, linking fixed points. WSS topological skeleton features allow the identification of flow features like flow stagnation, recirculation and separation which are classified as “aggravating” biomechanical events, linked to “aggravating” biological events. Among the aggravating biological events for atherosclerosis onset/progression, mass transport processes are markedly involved by mediating, e.g., the accumulation of lipids at the arterial wall. Mass transport mechanism, are, in turn, influenced by local hemodynamics, which may promote, e.g., low-density lipoproteins (LDL) and monocyte receptor expression on the endothelium. These mechanisms are causally related to the development of the disease (Tarbell et al., 2013). For this reason, Lagrangian-based features of WSS topological skeleton has been suggested to provide a

template of near-wall mass transport. However, the complexity of the Lagrangian-based method requires high computational costs. To overcome this limitation, a Eulerian method to analyse WSS topological skeleton has been recently proposed by Mazzi and co-workes. In this contest, the aim of this work was to test the ability of the recently proposed Eulerian-based features of WSS topological skeleton to provide a template of blood-to-wall LDL transfer, in patient-specific computational models of human arteries.

Chapter 2

Materials and Methods

This chapter gives a detailed overview of all the steps followed to conduct the study: from models reconstruction from clinical data to LDL-transport simulation and data post-processing. The workflow with all the followed phases of the work is reported in *figure 2.1*. In detail, starting from clinical data, a mesh was generated for each cardiovascular district (selected by a *sensitivity analysis*) and boundary and initial conditions were set to properly simulate mass transport and fluid motion. Two unsteady-state simulations were run, one for each model, and results were post-processed in terms of LDL luminal concentration and WSS-based hemodynamic quantities.

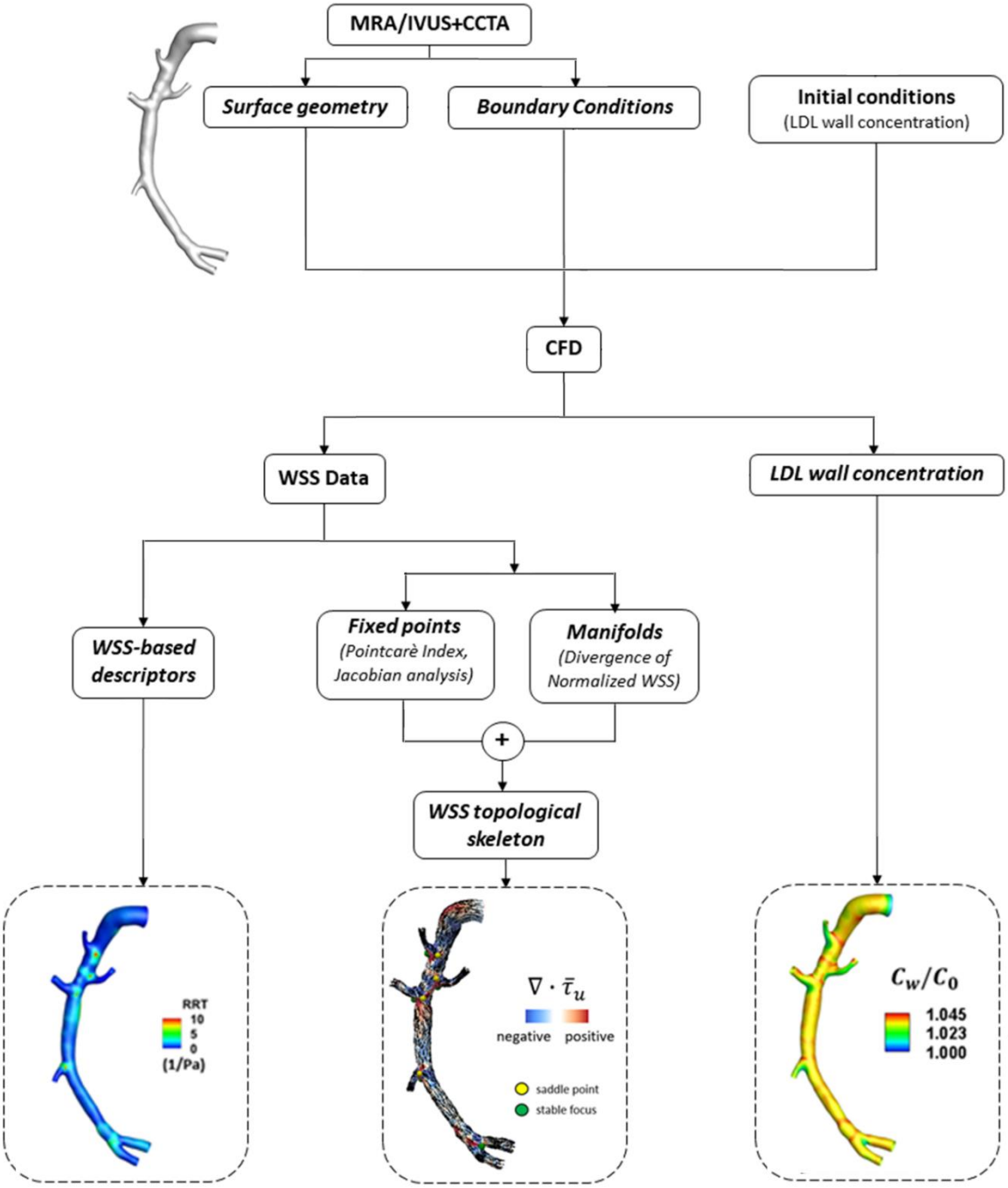

Figure 2.1 Overview of the applied methods. The workflow reports the main steps of the study.

2.1 Computational model

2.1.1 Geometry reconstruction

The geometries of one carotid bifurcation and one right coronary artery were reconstructed from medical images of two different ostensibly healthy subjects (*figure 2.2*).

In detail, the carotid artery was reconstructed from Contrast Enhanced Magnetic Resonance Angiography (CE MRA) images by using the Vascular Modelling Toolkit environment (vmtk), as detailed elsewhere (Steinman et al., 2002). The resulting model consists of the common carotid artery (CCA), the internal (ICA) and the external (ECA) carotid artery districts. Flow extensions were added at the inlet and outlets section of the reconstructed geometry to avoid boundary effects. As in previous studies (De Nisco et al., 2019, 2020a; Hoogendoorn et al., 2020) the right coronary artery, it was reconstructed from Intra Vascular Ultrasound (IVUS) and a Coronary Computed Tomography Angiography (CCTA) images. More in detail, the lumen contours of the vessel were semi-automatically segmented on the IVUS images and then aligned along the CCTA lumen centerline. The side

branches were reconstructed with a length of at least 1 diameter to avoid boundary effects.

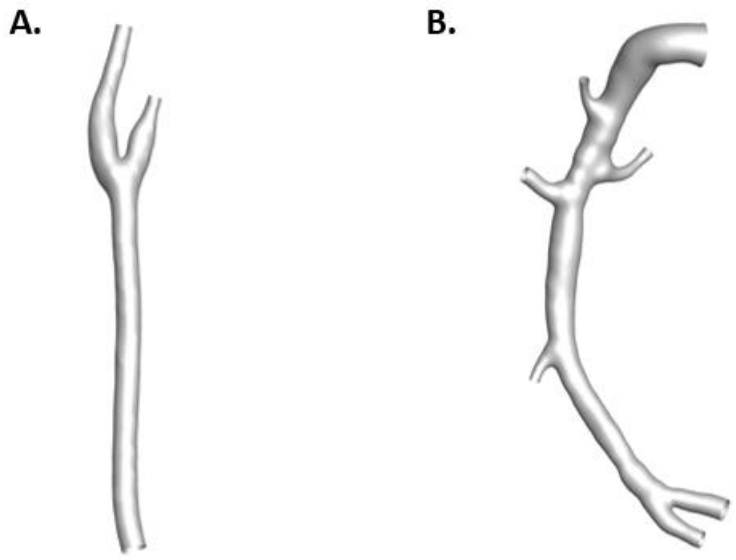

Figure 2.2 A representation of the reconstructed geometries of the carotid bifurcation (**A**) and the right coronary (**B**).

2.1.2 Model meshing

To numerically solve the problem governing equations, models were meshed by using ICEM (ANSYS Inc.). In detail, following an approach proposed by De Nisco and co-workers (2018), each vascular district was discretised by means of tetrahedrons in the bulk and 30-layers of high-quality prismatic cells in the boundary layer. A sensitivity analysis was conducted to properly set the best grid assuring mesh-

independency and good accuracy of the results, with acceptable computational costs. I In detail, steady-state simulations were performed on six computational grids with different cardinality (from about 1M to 7M elements) for each vascular district by using the CFD general code Fluent (Ansys Inc.) The resulting meshes had the following size:

Cardiovascular District	**Cardinality**	**Tetrahedral Elements**
Carotid Bifurcation	6,100,000	1,500,000
Right Coronary Artery	4,000,000	930,000

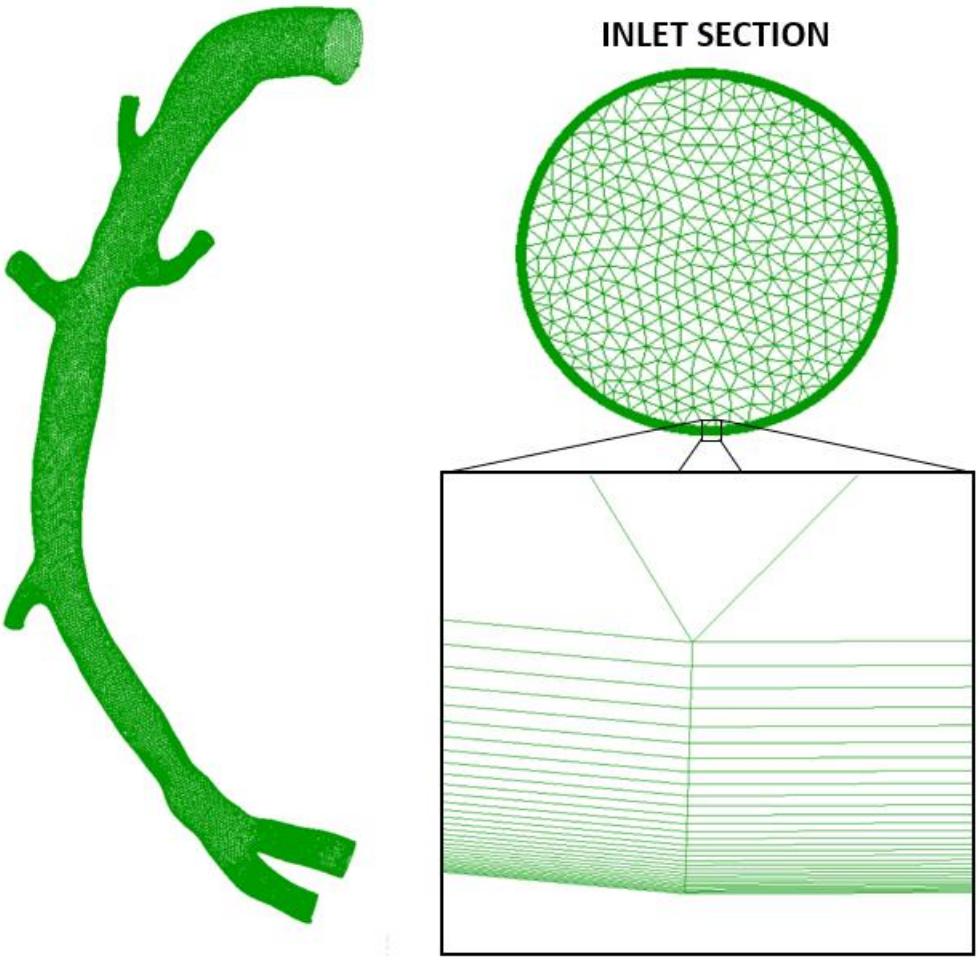

Figure 2.3 A representation of the resulting computational grid of the RCA. A view of the inlet section is provided at the right panel with a zoom at the boundary layer.

The accurate discretization of the near-wall region, needed to properly simulate LDL transport and blood-to-wall transfer, based on the *Peclet number* (Pe) (Tada 2010; Li et al., 2017; De Nisco et al., 2018). The average *Peclet number*

is the product of the average *Reynolds number* (Re) and *Schmidt number* (Sc) and it represents the proportion of convection to diffusion. It is described by the following equation:

$$Pe = Re \cdot Sc = \frac{D_h U}{v} \frac{v}{D_{ldl}} = \frac{D_h U}{D_{ldl}} \quad (2.1)$$

were D_h and U represents, respectively, the hydraulic diameter and the mean velocity value at the inflow section averaged along the cardiac cycle. D_{ldl}, the diffusivity of the LDL in flowing blood, was set to a constant value of $5{,}8 \cdot 10^{-12}\ m^2 s^{-1}$ (Wada and Karino, 2002). The design of the near-wall computational grid made up by high-quality prismatic elements, was driven by theory (Tada, 2010). In detail, to properly represent the mass transfer of LDL through the vessel wall, it is necessary to have a very refined computational grid, with a grid size dimension Δr_{max} close to the luminal surface, defined as:

$$\Delta \mathrm{r}_{max} = \frac{\delta_c}{3} = \frac{\delta}{3 \cdot \sqrt[3]{Sc}} = \frac{2.28 \cdot \sqrt{2\nu/\omega}}{3 \cdot \sqrt[3]{Sc}} \quad (2.2)$$

$$Sc = \frac{\mu}{\rho \cdot D_{ldl}} = \frac{v}{D_{ldl}} \tag{2.3}$$

where δ_c is the LDL boundary layer thickness, δ is the boundary layer thickness of the pulsatile flow, ω is the pulsation of the cardiac cycle, *Sc* is the Schmidt number, ρ is the density of blood and μ and v are respectively the dynamic and kinematic viscosity. All the measurement and sizes for the two cardiovascular districts obtained in the study are represented in *table. 2.1*. It is pointed out that the adopted wall grid size for the study was *27 times smaller* than the Δr_{max} needed to describe mass transfer of LDL through the wall. This choice was made to assure that the simulations of LDL blood-to-wall transfer were not affected by the quality of the mesh grid.

Table 2.1 Resulting Peclet, Reynolds and Schmidt numbers for each cardiovascular district. Resulting $\boldsymbol{\Delta r_{max}}$ and $\frac{\boldsymbol{\Delta r_{max}}}{27}$ are also reported.

Cardiovascular District	*Common Carotid*	*Right Coronary Artery*
Peclet Number	$2.99 \cdot 10^{8}$	$9.36 \cdot 10^{7}$
Reynolds Number	542.6139	$1.7 \cdot 10^{2}$
Schmidt Number	$5.52 \cdot 10^{5}$	$5.52 \cdot 10^{5}$
$\boldsymbol{\Delta r_{max}}$ $[\boldsymbol{m}]$	$2.35 \cdot 10^{-3}$	$2.26 \cdot 10^{-5}$
$\frac{\boldsymbol{\Delta r_{max}}}{\boldsymbol{27}}$ $[\boldsymbol{m}]$	$2.7 \cdot 10^{-7}$	$8.36 \cdot 10^{-7}$

2.2 Numerical approach

LDL mass transport in the streaming blood and his transfer through the wall was modelled by coupling the governing equation of fluid motion (Navier-Stokes) with the advection-diffusion equation under unsteady flow condition.

2.2.1 Fluid dynamic problem formulation

The Navier-Stokes momentum equation and the continuity equation are the governing equation of fluid motion. The governing equations expressed in differential form are:

$$\begin{cases} \frac{\partial(\rho u)}{\partial t} + \nabla \cdot \rho u u + \nabla p = \nabla \bar{\bar{\tau}} + \rho f_v \\ \frac{\partial \rho}{\partial t} + \nabla \cdot (\rho u) = 0 \end{cases} \qquad \text{(2.4) and (2.5)}$$

where u and p represent, respectively, the fluid velocity vector and the pressure, ρ is the blood density and ρf_v represent the volume forces. Equation (2.4) is the Navier-Stokes momentum equation and is derived from the momentum conservation equation extended to unsteady-state systems:

$$\begin{gathered}\boldsymbol{rate\ of} \\ \boldsymbol{momentum\ accumulation} = \\ \boldsymbol{in\ the\ control\ volume\ CV}\end{gathered}$$

$$\begin{gathered}\boldsymbol{rate\ of} \\ \boldsymbol{momentum} \\ \boldsymbol{entering\ CV}\end{gathered} - \begin{gathered}\boldsymbol{rate\ of} \\ \boldsymbol{momentum} \\ \boldsymbol{leaving\ CV}\end{gathered} + \begin{gathered}\boldsymbol{sum\ of\ forces} \\ \boldsymbol{acting\ on} \\ \boldsymbol{the\ system}\end{gathered}$$

The left side of the equation represents the acceleration while the right side is the sum of all body forces (i.e. gravity force) and divergence of deviatory stress. The second equation of the system (2.5) is the general form of the mass continuity equation which states that the rate of mass accumulation in the control volume (CV) is the exact sum of the mass entering and the mass leaving the control volume:

$$\begin{gathered}\boldsymbol{rate\ of\ mass} \\ \boldsymbol{accumulation} = \\ \boldsymbol{in\ the\ CV}\end{gathered} \begin{gathered}\boldsymbol{rate\ of} \\ \boldsymbol{mass} \\ \boldsymbol{entering\ CV}\end{gathered} - \begin{gathered}\boldsymbol{rate\ of} \\ \boldsymbol{mass} \\ \boldsymbol{leaving\ CV}\end{gathered}$$

A Newtonian behaviour was assumed for blood in the carotid bifurcation. Consequently eq. (2.4) and (2.5) are altered because fluid density and dynamic viscosity are assumed to be constant and the term $\nabla\bar{\bar{\tau}}$ becomes equal to $\mu\nabla^2 u$. The resulting equation are simplified as follows:

$$\begin{cases}\rho\left[\frac{\partial u}{\partial t} + u(\nabla \cdot u)\right] = -\nabla p + \mu\nabla^2 u + \rho g \\ \nabla \cdot u = 0\end{cases} \qquad \text{(2.6) and (2.7)}$$

where the gravity force is considered to be the only volume force. These are coupled, non-linear, partial differential equations where the unknow variables are the blood velocity vector u and the pressure p. These equations are defined in two computational domains defined as Ω where the walls, inlet surfaces and outlet surface are indicated, respectively, with Γ^w , Γ^{in} and Γ^{out} (*figure 2.4*).

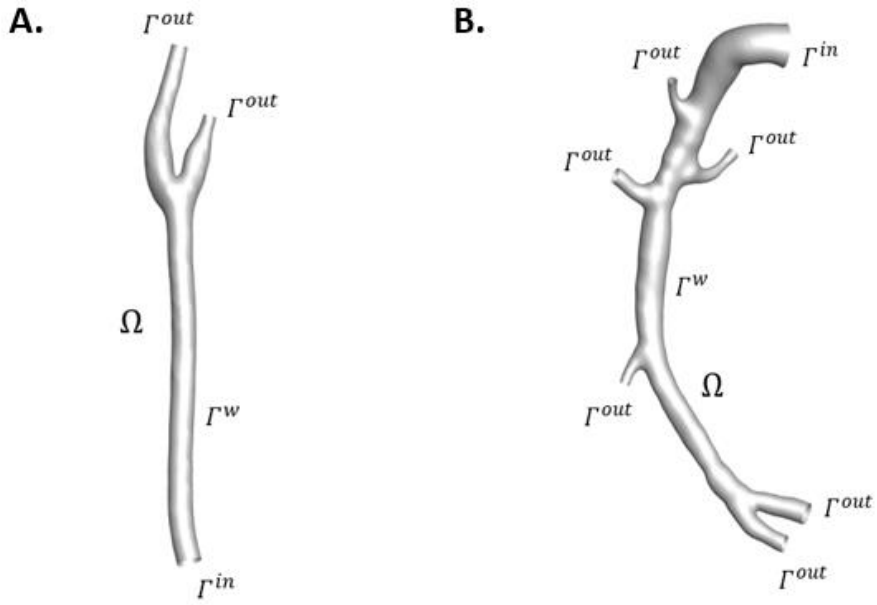

Figure 2.4 A representation of the two analysed computational domains reconstructed in the Vascular Modelling Toolkit environment (VMTK).

2.2.2 LDL transport problem formulation

LDL was assumed to be dissolved in blood and consequently modelled as a passive non-reacting scalar, transported in the bloodstream according to the following advection-diffusion equation:

$$\frac{\partial C}{\partial t} + u \cdot \nabla C - D_{ldl} \nabla^2 C = 0 \qquad (2.8)$$

where C is the LDL concentration in blood and u is the velocity vector, obtained from the Navier-Stokes equations. More in detail, the time-dependent behaviour of the LDL concentration in blood is represented by the non-stationary term $\frac{\partial C}{\partial t}$; $u \cdot \nabla C$ is the advective/convective term and it represents the variation in LDL concentration at a given location because of the flow and $-D_{ldl} \nabla^2 C$ is the diffusive term representing the transport of LDL in flowing blood due to diffusion (it is proportional to the second derivative of concentration C). To solve the mass transport equation in the Fluent environment, the definition of a *User-Defined Scalar* is required (*uds*). The *uds* represent the LDL concentration in the analysed fluid domain and the corresponding equation

was activated and customized in Fluent by setting the D_{ldl} parameter (*uds* diffusivity in blood) to $6.3 \cdot 10^{-9}\ kg\ m^{-1}s^{-1}$.

2.2.3 Simulation assumptions

2.2.3.1 Rheological model

Blood was treated as a homogeneous, isotropic, incompressible, Newtonian viscous fluid with specific mass ρ equal to 1060 $kg\ m^{-1}$ and dynamic viscosity μ set to a constant value of 0.0035 $Pa \cdot s$. If each component of the stress tensor $\bar{\bar{\tau}}$ is treated like a linear isotropic function of velocity gradient (∇u) components, for an incompressible fluid, the following equation is considered valid:

$$\bar{\bar{\tau}} = 2\mu D(u) \tag{2.9}$$

where $D(u)$ is the rate of deformation tensor. Equation (2.9) explains the relation between shear stress and shear rate which are directly proportional (it is a linear relation) for a Newtonian fluid if a constant dynamic viscosity of the fluid (μ) is defined. Equation (2.9) can now be written as follows:

$$\bar{\bar{\tau}} = \mu\dot{\gamma} \tag{2.10}$$

The assumptions made on the blood (Newtonian fluid with constant density and dynamic viscosity) are considered acceptable to analyse specifics cardiovascular districts, even if they do not represent the reality of the fluid. It has been proved that modelling blood as a Newtonian fluid carries to negligible errors in the solution when the district has a large diameter and is exposed to higher shear rates. For this reason, the Newtonian assumption, even with his limitations, was considered acceptable to study and analyse the *common carotid*. Otherwise, a different assumption was made for the *right coronary* because of the small diameter of the district. For cardiovascular districts with a diameter less than 500 µm, the assumption of a Newtonian fluid is no longer completely correct, and a non-Newtonian rheological model must be used. The most common type of non-Newtonian behaviour is the *shear thinning* which consist in the decrease of viscosity with the increase of the shear rate $(\mu(\dot{\gamma}))$. The rheological model used in this study to analyse the *right coronary* is the *Carreau* model described by the following equation:

$$\mu(\dot{\gamma}) = \mu_\infty + (\mu_0 - \mu_\infty)[1 + (\lambda\dot{\gamma}^2)]^{\frac{n-1}{2}} \quad (2.11)$$

where μ_0 in the initial viscosity at a shear rate value of 0 (set to $0.25\,\frac{kg}{ms}$), μ_∞ is the viscosity of a Newtonian fluid (set to $0.0035\,\frac{kg}{ms}$), n is the Power-Law Index (here 0.25) and λ is the relaxation time constant (25 s).

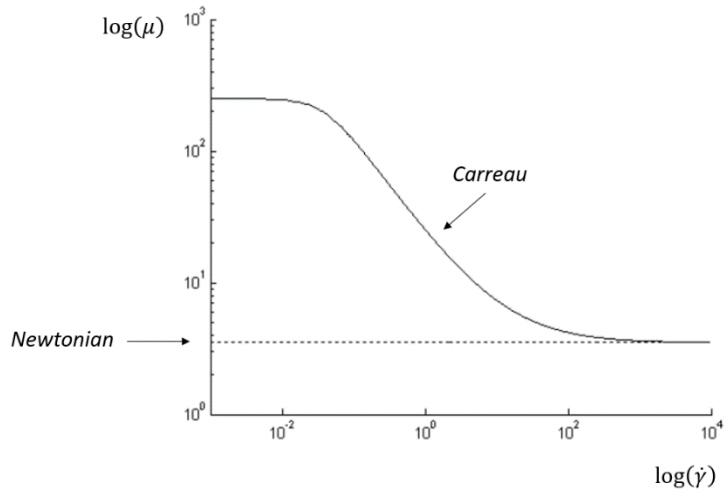

Figure 2.5 A representation of the dependence of the viscosity from the shear rate for the Carreau and Newtonian models.

Blood flow was considered laminar, without considering the turbulence and its effects on LDL transfer through wall for both the analysed cardiovascular districts. The characterization of the flow regimes is based on a

dimensionless quantity known as Reynolds number, which, for a flow in a pipe, is defined as follows:

$$Re = \frac{\rho U D}{\mu} \tag{2.12}$$

where D is the diameter of the inflow section of the analysed cardiovascular district. Reynolds number represent the ratio of inertial forces over viscous forces. According to this definition, low Reynolds numbers characterize regimes where viscous forces prevail over inertial forces (laminar regimes) and high Reynold numbers characterize regimes where inertial forces prevail over viscous forces (turbulent regimes). In the case of flow in a cylindric pipe, based on the Reynolds number, three different regimes have been identified:

- Re ≤ 1000 → laminar flow;
- 1000 ≤ Re ≤ 2000 → transition regime;
- Re ≥ 2000 → turbulent flow.

According to the values previously shown in *table 2.1*, the assumption of laminar flow is considered valid. Straight flow extensions were added at the outlets and inlet sections of the

common carotid to ensure a fully developed flow and to minimize the effect of the boundary conditions on the solution while no flow extensions were added at the right coronary artery since side-branches of at least one diameter long were considered to be enough to avoid boundary effects.

2.2.3.2 Boundary Conditions

To properly solve the fluid dynamic and mass transport problem, it is necessary to set appropriate boundary conditions on the cardiovascular districts. As previously stated and shown in *figure 2.4*, Γ^w represent the wall of the vessels and it is the physical border of the model while Γ^{in} and Γ^{out} are the inlet and outlet surfaces. These are fictious surfaces arbitrarily created by clipping the original model perpendicularly to the centrelines to close the cardiovascular districts and separate them from the rest of the cardiovascular system in order to make a more accurate analysis. As for the fluid dynamic problem, the *carotid bifurcation* and the *right coronary artery* walls were assumed

to be rigid with no-slip condition al the wall. Measured flow rate were imposed at the inlet section of each model in terms of flat velocity profile (Gallo et al., 2018; De Nisco et al., 2019,2020). The time-dependent flow rates imposed at the CCA and RCA inlet sections are reported in *figure 2.7.*

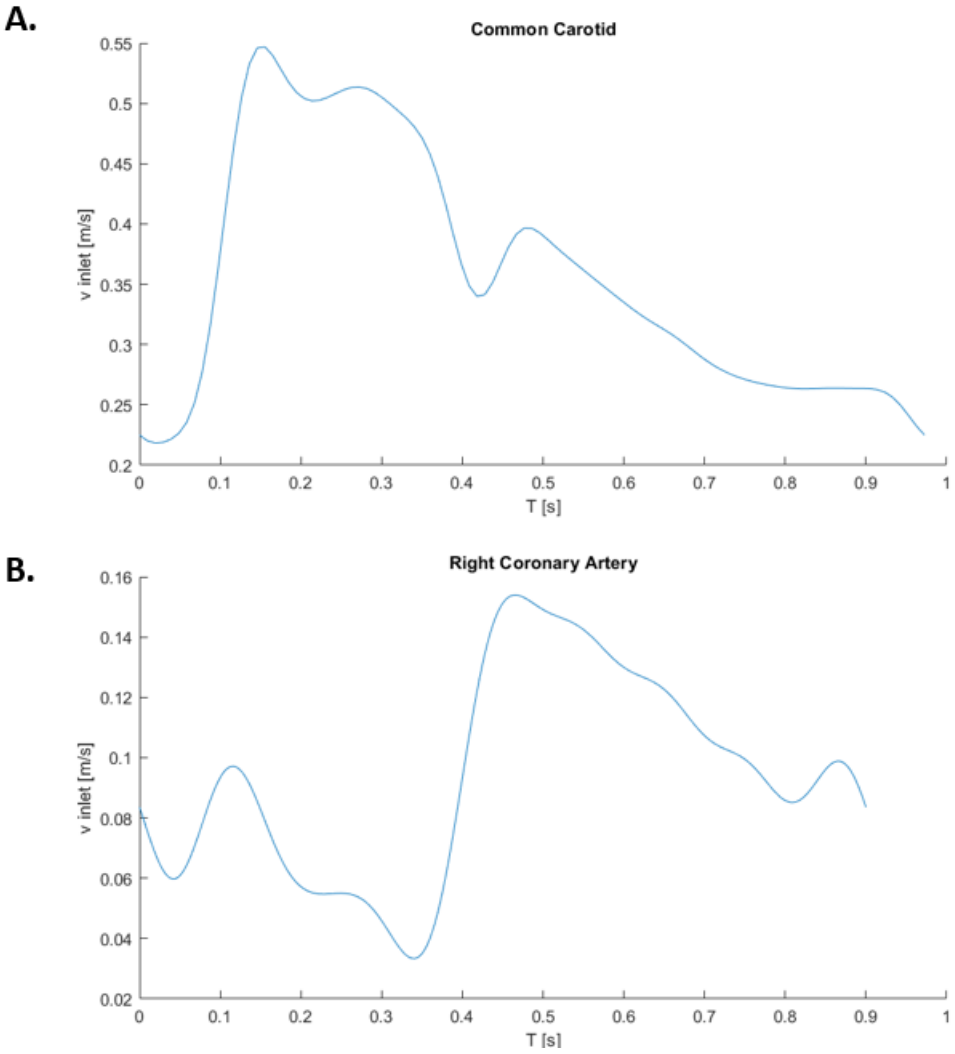

Figure 2.6 A representation of the velocity inlet values of the *common carotid* (**A**) and the *right coronary artery* (**B**).

Figure 2.6 A displays the time-dependent trend of the *common carotid* artery inlet velocity, with a period of $0.972\ s$, corresponding to a cardiac frequency of $58\ bpm$.

Figure 2.6 B represents the time-dependent velocity profile prescribed at the inlet surface of the *right coronary artery*, with a cardiac period of $0.9\ s$ ($54\ bpm$). Measured inflow rates were imposed in terms of flat velocity profile at the inlet section of the vessels. This assumption is acceptable since the analysis was focused at a vascular district enough distally with respect to the inlet section of each model. The time-dependent flat velocity profile was imposed by defining specific *User-Defined Function* (*udf*), loaded in Fluent (ANSYS Inc.),computing the velocity value by dividing the instantaneous flow rate by the inlet section area for each simulation time-step. As regards the outlet sections of the models, at the ICA the measured mass flow rate was imposed in terms of mass flux defined as:

$$MassFlux(t) = \frac{-vfr_{ICA}(t)\cdot\rho}{A} \tag{2.13}$$

where vfr_{ICA} represents the volumetric flow rate at the outlet section, ρ is the density of blood and A is the area of the outlet section. The ECA outlet was set to a reference constant pressure value of 0 to make the simulation calculate automatically the mass flow rate (Gallo et al., 2018). As for

the *right coronary* artery, based of measurements availability, measured or estimated flow ratios were imposed as outlet boundary conditions (De Nisco et al., 2019, 2020; Hoogendoorn et al., 2020). In detail, at each side branch the mean flow rate was derived from upstream and downstream flow rate measurement and applied in terms of percentage of inlet flow rate. If measurements were not available or not good enough, the flow rate ratio to impose was estimated by using a scaling low based on diameters (van der Giessen et al., 2011). The imposed flow ratios are reported in *figure 2.7*. To solve equation (2.5), an equal approach was used for both the analysed cardiovascular districts. LDL concentration C was considered to be the ratio between the LDL concentration at the wall C_w and the initial LDL concentration C_0 (C_w/C_0). The blood-to-wall transport was defined by an *udf* with the following equation (De Nisco et al., 2018):

$$C_w V_w - D_{ldl} \left.\frac{\partial C}{\partial n}\right|_w = K_w C_w \qquad (2.14)$$

where C_w is the LDL concentration at the wall, V_w is the water filtration velocity at the wall, $\frac{\partial C}{\partial n}$ is the concentration gradient

normal to the wall (n is the direction normal to the luminal surface) and K_w is the overall mass transfer coefficient of LDL at the vessel wall. Equation (2.14) states that the amount of LDL infiltrating into the vessel wall is equal to the difference between the amount carried to the vessel by filtration and the amount sent back to the bloodstream and it represent the "mass balance at the wall-blood interface". A constant LDL concentration equal to C_0 was set at the inlet section of each model, while a stress-free condition was imposed at each outlet section (De Nisco et al., 2018).

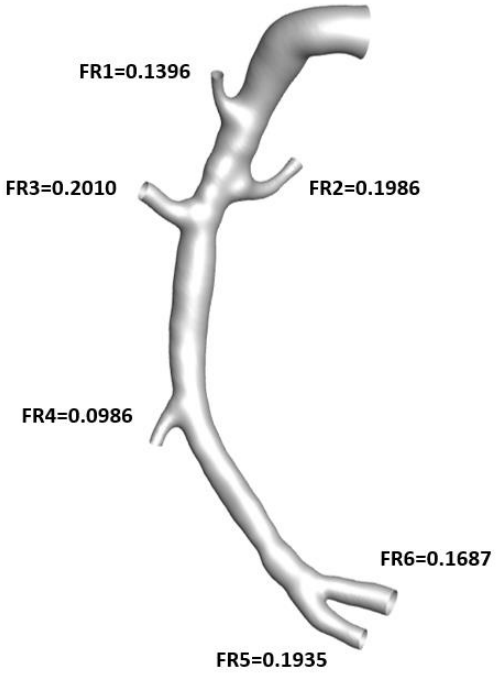

Figure 2.7 A representation of the constant outflow ratios imposed at each outlet of the right coronary artery.

2.2.3.3 LDL Initial Conditions

Based on previous evidence on the impact of initial LDL concentration on simulation results and computational costs (De Nisco et al., 2018), a proper initial LDL concentration was imposed for unsteady-state simulation as a uniform LDL concentration in the whole domain equal to C_0.

2.2.4 Computational settings

Summarizing, two unsteady-state simulation were performed, one for each model. Second order accuracy was prescribed to solve both the momentum and pressure equations in order to achieve higher-order accuracy at cells faces. The backward Eulerian implicit scheme was adopted for time integration, with a fixed time step value of $0.001\ s$. The blood flow in the *carotid bifurcation* was simulated along its cardiac cycle ($58\ bpm$) corresponding to 972 time-steps while the right coronary artery ($54\ bpm$) was simulated for 900 time-steps. A maximum number of 150 iterations was set for each time-step.

2.2.5 Post-processing

To properly analyse and quantify LDL polarization and identify the most probable location for the insurgence of atherosclerosis, near-wall hemodynamics was evaluated in terms of different hemodynamics descriptors which were calculated and displayed. The descriptors used in this study are described in detail in the following sections.

2.2.5.1 Classical WSS-based descriptors

WSS-based descriptors were used to analyse the distribution of LDL at the wall. In detail, three of the most widely WSS-based descriptors were computed: *time-averaged wall shear stress* (TAWSS), *oscillatory shear index* (OSI) (Ku et al., 1985) and *relative residence time* (RRT) (Himburg et al., 2004). These descriptors were computed as follows:

$$TAWSS = \frac{1}{T}\int_0^T |\boldsymbol{WSS}| \cdot dt \qquad (2.15)$$

$$OSI = 0.5\left[1 - \left(\frac{\left|\int_0^T \boldsymbol{WSS}\cdot dt\right|}{\int_0^T \boldsymbol{WSS}\cdot dt}\right)\right] \quad 0 \le OSI \le 0.5 \qquad (2.16)$$

$$RRT = \frac{1}{TAWSS\cdot(1-2\cdot OSI)} = \frac{1}{\frac{1}{T}\left|\int_0^T \boldsymbol{WSS}\cdot dt\right|} \qquad (2.17)$$

where T is the cardiac cycle and $\boldsymbol{WSS}$ is the wall shear stress vector. These descriptors allow to identify the zones characterized by "disturbed" flow over the vessel surface. TAWSS represents the values of WSS magnitude mediated over the cardiac cycle. Low TAWSS values (lower than 0.4 Pa) are known to stimulate proatherogenic endothelial phenotype, moderate TAWSS values (greater than 1.5 Pa) induces quiescence and an atheroprotective gene expression profile while higher TAWSS values (relevant from 25-45 Pa) can lead to endothelial trauma (Malek et al., 1999). OSI quantifies the oscillation of WSS vectors over the surface and it is used to locate zones characterized by an over-oscillation which appear to be correlate with perturbed endothelial alignment (He and Ku, 1996). Low OSI values occur where flow disruption is minimal while high OSI values (with a

maximum of 0.5) identify region where the instantaneous deviations of the WSS from the main flow direction induce a chance in the endothelial alignment. RRT is a combination of TAWSS and OSI. It is proportional to the residence time of blood particle near the wall, inversely proportional to the magnitude of the TAWSS vector and identify zones with low and oscillatory WSS values.

2.2.5.2 WSS topological skeleton

As previously stated, a recent study based on the analysis of the WSS topological skeleton with a Eulerian-based method (Mazzi et al., 2020, De Nisco et al., 2020b, Morbiducci at al., 2020) was here considered. In detail, the WSS topological skeleton is composed by *WSS fixed points* (where WSS vector vanishes) and *WSS manifolds* (regions of contraction and expansion) which connect the fixed points. Through the Volume Contraction Theory, normalized *divergence* was discovered to give practical information about a dynamic system if computed on the vector field associated with the system. In detail, it can be demonstrated that WSS divergence characterize the behaviour of the phase-space in

the infinitesimal neighbourhood of a trajectory and consequently can be used to identify the connections between fixed points (i.e. manifolds).

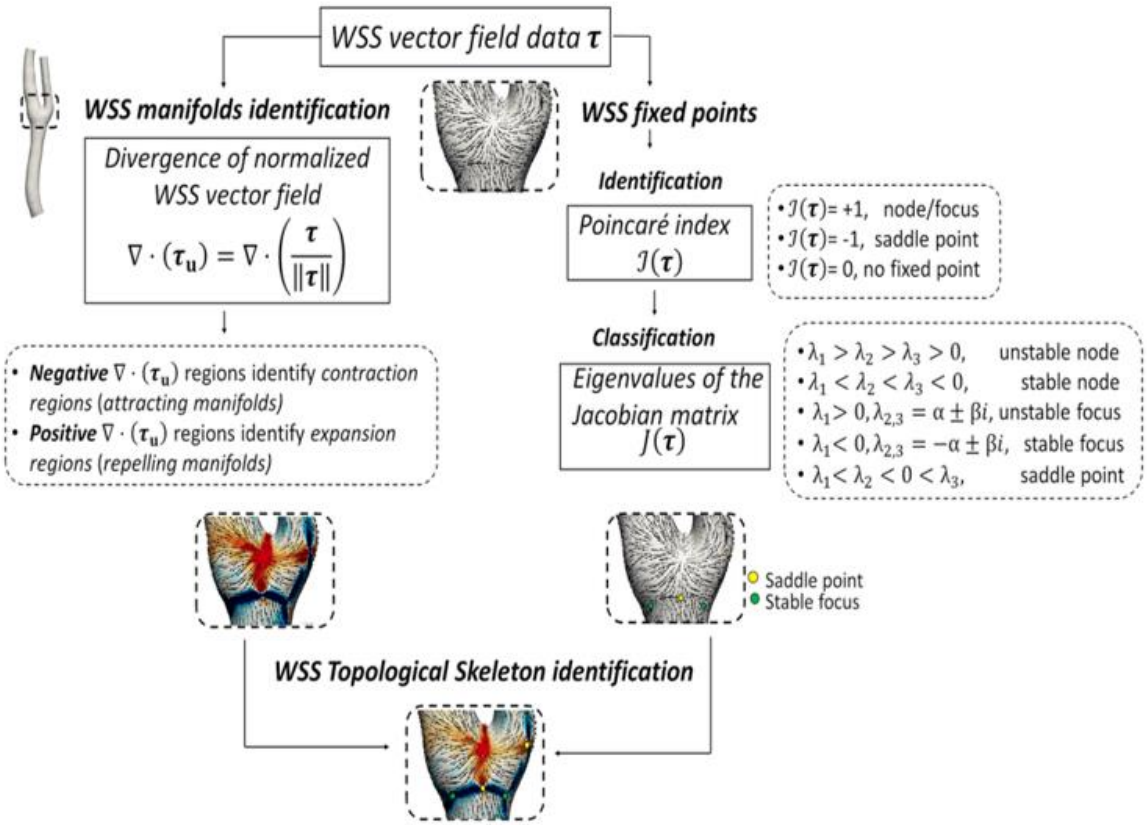

Figure 2.8 An overview on the WSS topological skeleton identification based on the analysis of manifolds by computing divergence of normalized WSS vector field and on the identification of WSS fixed points by the analysis of the Poincaré index (Mazzi et al., 2020).

As displayed in *figure 2.8*, the first step was to compute the divergence of the normalized WSS vector field in order to identify the WSS manifolds. Positive values of divergence identify expansion regions (repelling manifolds) while negative values of divergence identify contraction regions (attracting manifolds). WSS fixed points were then calculated by identifying the Poincaré Index, which points out nodes where the WSS vector vanishes. The nodes were then classified based on the eigenvalues of the Jacobian matrix as (a) stable/unstable nodes, (b) stable/unstable focus or (c) saddle points. The analysis was here based on the computation of the divergence of the WSS vector field allowing to identify the chance of direction of the WSS vectors over the cardiac cycle and consequently, to detect regions of contraction and expansion (i.e. manifolds) on the luminal surface of the vessels. According to the method described by Mazzi et al. in 2020, the divergence of the normalized WSS vector field was computed as follows:

$$DIV = \nabla \cdot \tau_u = \nabla \cdot \left(\frac{\tau}{\|\tau\|_2} \right) \tag{2.18}$$

where τ_u is the WSS unit vector. In detail, negative values of DIV identify contraction regions (which well approximates unstable manifolds) while positive values of DIV identify expansion regions (representing the stable manifolds). The choice to use the normalized vector of WSS was made in order to not consider the magnitude variation of the WSS vector and therefore correctly identify the unstable manifolds. The WSS topological skeleton analysis was computed to prove the existence of a strong co-localization between contraction regions and LDL luminal polarization.

2.2.5.3 Similarity analysis

In order to evaluate the ability of the analysed hemodynamic descriptors as marker for LDL polarization, a threshold was chosen for each descriptor, using a scheme already proposed (Gallo et al., 2016; De Nisco et al., 2018). In detail, luminal surface areas exposed to “disturbed hemodynamics” were identified by computing objective thresholds as the 10^{th} percentile for TAWSS and the 90^{th} percentile for OSI and RRT. Luminal region exposed to WSS contraction action along

the cardiac cycle were identified by values of DIV lower than the 10^{th} percentile of luminal DIV distribution. These luminal surface areas were named as TAWSS10, OSI90, RRT90, and DIV10, respectively. . In addition, the luminal LDL polarization was identified by luminal LDL concentration higher than the 90^{th} percentile of LDL wall distribution. The latter was named as LDL90.

The co-localization between critical values of descriptors and LDL polarization was then quantified in terms of *Similarity Index* (SI), described by the following equation (Gallo et al., 2016):

$$SI = \frac{2\left(SA_{LDL90} \cap SA_j\right)}{SA_{LDL90} + SA_j} \tag{2.19}$$

where SA is the surface area and j is used to identify all the critical regions (i.e. TAWSS10, OSI90, RRT90 and DIV10). The similarity Index allows us to well quantify the best descriptor, among the analysed one, to be used as an appropriate marker of LDL luminal polarization.

Chapter 3

Results

The results of the study are reported in the following. For each investigated model, the analysis was focused at the regions of interest, by clipping model extremities. In detail, as for the *carotid artery model*, the analysis involved the carotid bifurcation region, isolated by clipping the CCA, the ICA, and the ECA, respectively 7, 5, and 2 diameters distally to the centre of the bifurcation. As for the *right coronary artery*, all the side branches were clipped to focus the attention on the main branch.

3.1 LDL wall concentration

The resulting luminal distribution of normalized LDL concentration is reported in figure 3.1 and 3.2 for coronary bifurcation and right coronary artery models, respectively.

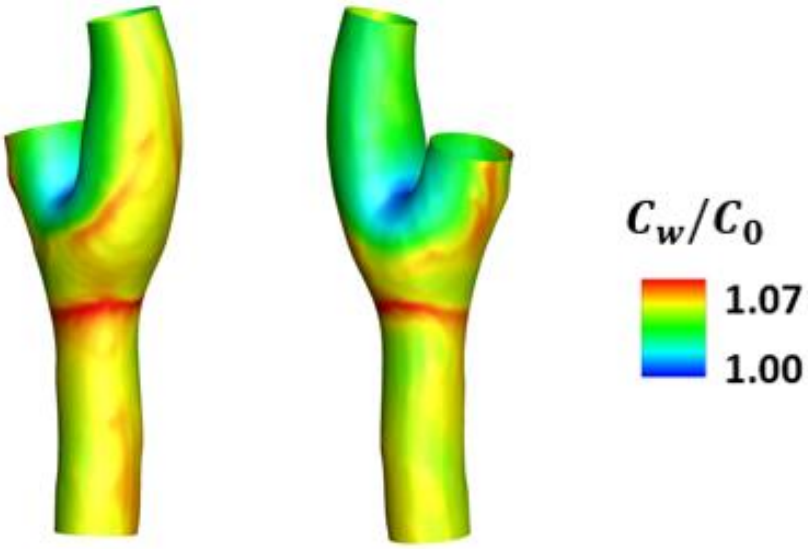

Figure 3.1 Distribution of normalized LDL concentration (C_W/C_0) at the luminal surface of carotid bifurcation.

In detail, as for the carotid bifurcation (*figure 3.1*), the luminal regions characterized by a high LDL uptake (red-coloured regions) appears to be mainly located at the basis of the carotid bifurcation and in small luminal areas along the outer walls of the ICA and ECA.

A low LDL concentration (blue/light blue regions) results only in a wide region at the apex of the carotid bifurcation.

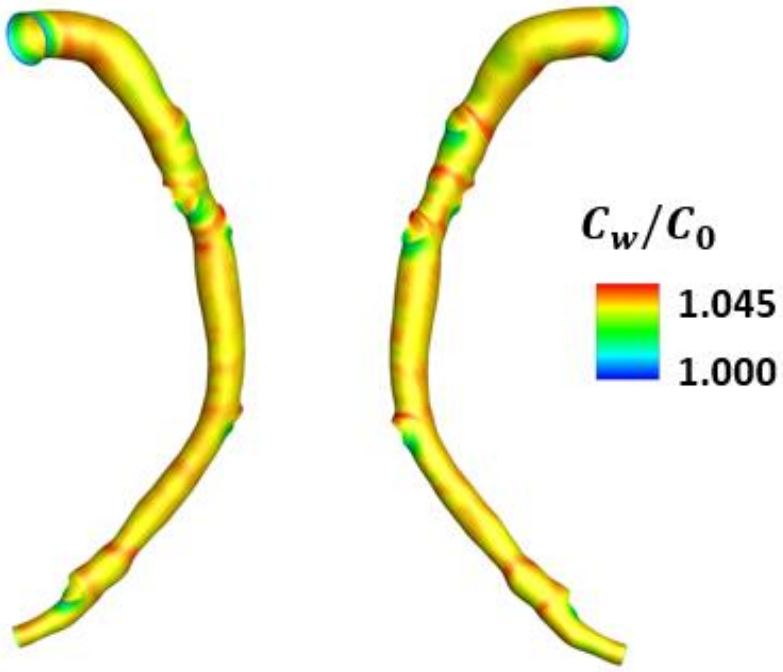

Figure 3.2 Distribution of normalized LDL concentration (C_W/C_0) at the luminal surface of the right coronary artery.

The LDL distribution on the luminal surface of the right coronary artery is presented in *figure 3.2*. As shown, LDL polarization regions occurred at several locations along the vessel and markedly co-localized with side branches entrance section. Only some spots of low LDL concentration (blue/light blue zones) characterize the luminal surface of RCA.

3.2 Classical WSS-based descriptors

A representation of the analysed WSS-based descriptors (TAWSS, OSI and RRT) is displayed in *figures 3.3* and *3.4*, respectively for coronary bifurcation and RCA models.

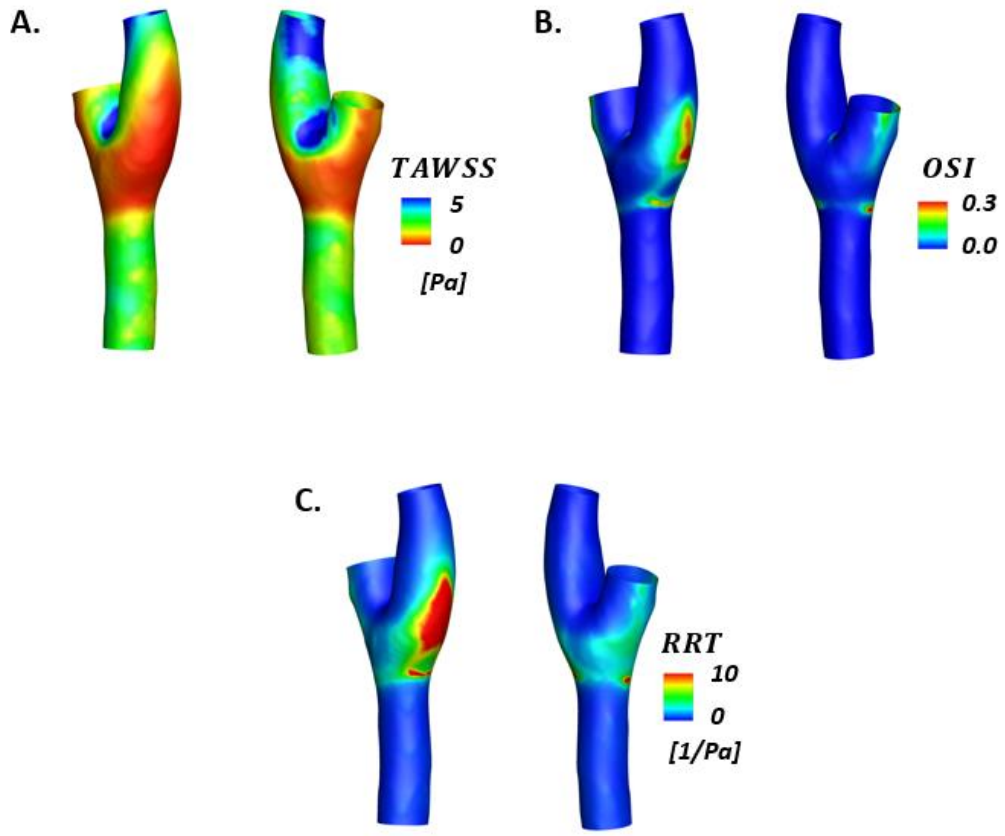

Figure 3.3 Luminal distribution of analysed WSS-based descriptors along the carotid bifurcation: (**A**) *time-averaged wall shear stress*, (**B**) *oscillatory shear index* and (**C**) *relative residence time* are displayed.

In detail, as for the *carotid artery*, in *figure 3.3-A* a wide region of low TAWSS values (red zone) is extended from the bottom of the carotid bifurcation to the outer wall of the ICA and ECA. Higher TAWSS values characterize the apex of the carotid bifurcation as well as the inner wall of the ICA.

Figure 3.3-B shows the OSI distribution along the luminal surface, identifying high OSI regions (yellow/red zones) at the basis of the carotid bifurcation, at the outer wall of the ECA, and at the carotid bulb along the outer wall of the ICA.

As concerns the RRT distribution, in *figure 3.3-C* a wide high region characterized by high RRT values (red zone) can be noted along the external wall of the ICA.

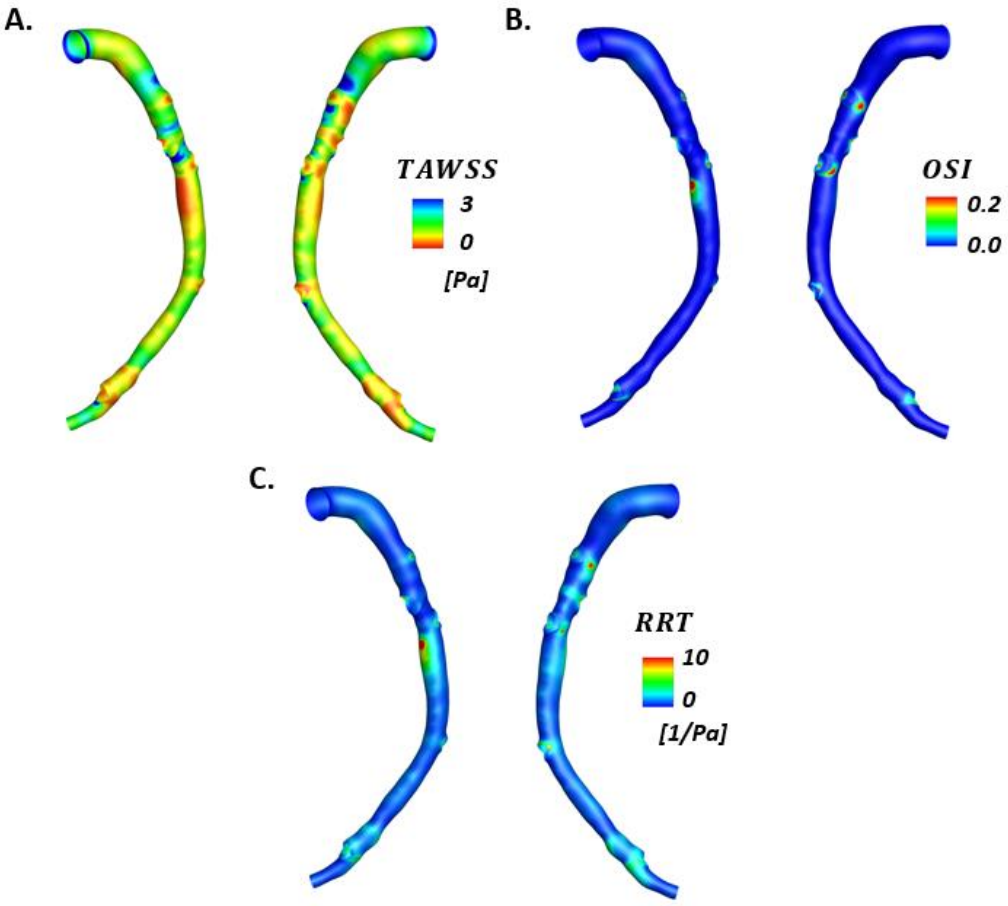

Figure 3.4 Luminal distribution of analysed WSS-based descriptors along the right coronary artery: (**A**) *time-averaged wall shear stress*, (**B**) *oscillatory shear index* and (**C**) *relative residence time* are displayed.

As for the *right coronary artery*, *figure 3.4-A* shows few appreciable regions of low TAWSS values (red zones) extended along the internal side of the vessel's curvature with a wider zone situated approximately in the middle of the

curvature. Higher TAWSS values characterize the inlet surface of the artery as well as at the entrance section of the first three side-branches of the artery.

Figure 3.4-B shows the OSI distribution along the luminal surface, identifying restricted high OSI regions (yellow/red zones) at the entrance section of the side-branches of the artery and one in the internal side of the curvature, approximately in the middle of the vessel.

As concerns the RRT distribution, *figure 3.4-C* highlight regions characterized by high RRT values (red zones) apparently co-localized with the ones shown in *figure 3.4-B* and characterized by a wider area.

3.3 WSS topological skeleton

The results of the WSS topological skeleton analysis are reported in *figures 3.5* and *3.6,* respectively for coronary bifurcation and RCA models.

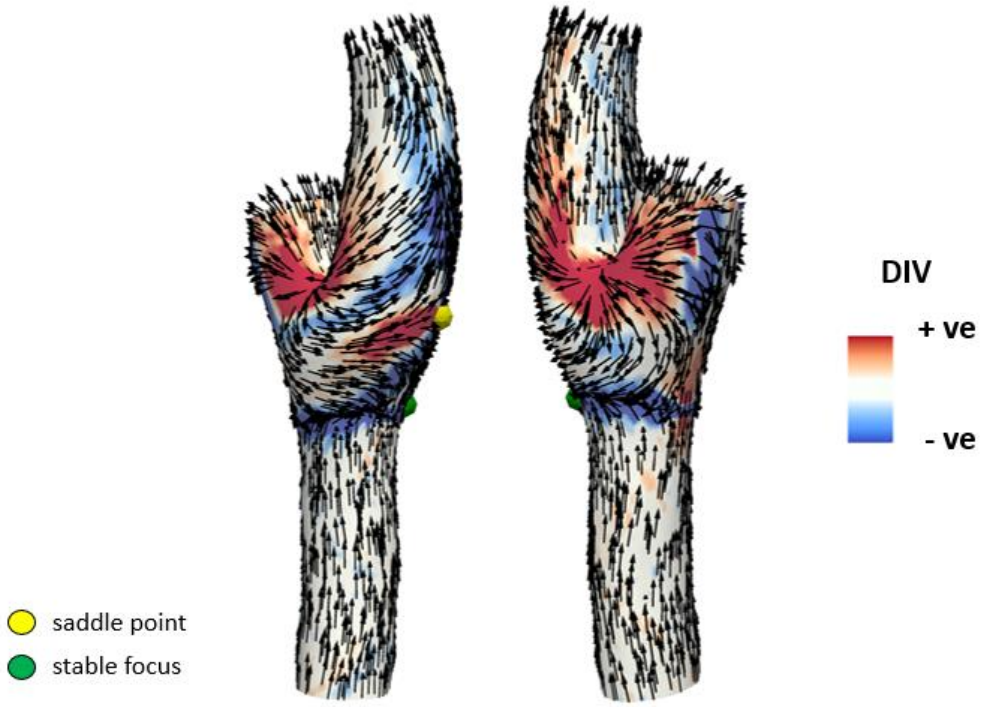

Figure 3.5 WSS topological skeleton of the carotid bifurcation. WSS manifold are coloured by red (repelling) or blue (attracting). Fixed points were classified as saddle points (yellow) and stable focus (green). Cycle-averaged WSS vector field is displayed by black arrows.

As represented in *figure 3.5*, in the carotid bifurcation WSS contraction regions (blue coloured) are mainly located at the basis of the bifurcation and along the outer walls of the ICA and the ECA. A wide WSS expansion region (red coloured) resulted at the apex of the carotid bifurcation.

As concerns WSS fixed points, a saddle point is located at the carotid bulb while a stable focus is located at the basis of the carotid bifurcation in a WSS contraction region.

Figure 3.6 WSS topological skeleton of the right coronary artery. WSS manifold are coloured by red (repelling) or blue (attracting). Fixed points were classified as saddle points (yellow) and stable focus (green). Cycle-averaged WSS vector field is displayed by black arrows.

Figure 3.6 represents the right coronary artery where the most significant result is the presence of contraction regions all along the inner curvature of the vessel while the external

side of the curvature presents a small quantity of expansion regions.

As concerns WSS fixed points, several saddle points are presented along the RCA luminal surface at the entrance section of the side-branches while a single stable focus is located at the entrance of the fifth side-branch (from the inlet section).

3.4 Co-localization of LDL with descriptors

3.4.1 WSS topological skeleton

WSS topological skeleton analysis pointed out critical regions on the vessels surfaces which were demonstrated to be correlated with disturbed flux zones, considered the first step that leads to the insurgence of cardiovascular diseases. For this reason, negative values of the divergence of the normalized WSS vector field were graphically compared to the LDL polarization on the vessel's walls to evaluate their co-localization.

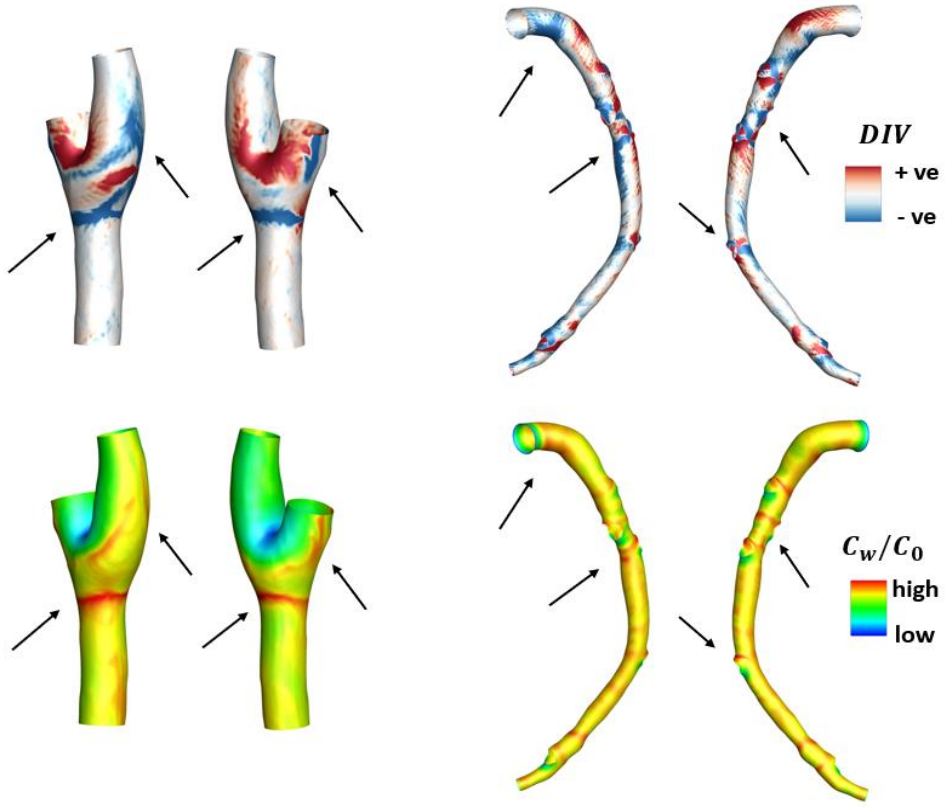

Figure 3.7 A representation of divergence of WSS vector field and LDL concentration over vessels walls with a focus on the similarity between the two representations.

As pointed out in *figure 3.7*, contraction regions on the *carotid bifurcation* and *right coronary* artery luminal surfaces, characterized by negative values of the divergence of the normalized WSS vector field, seem to be qualitatively co-localized with LDL high concentration regions along the vessel wall. In detail, a marked co-localization of WSS contraction regions and LDL polarization emerged at the

basis of the carotid bifurcation and along the external walls of the ICA and ECA for the carotid artery, and at the inner curvature of the vessel and at the entrance of each side-branches for the right coronary artery.

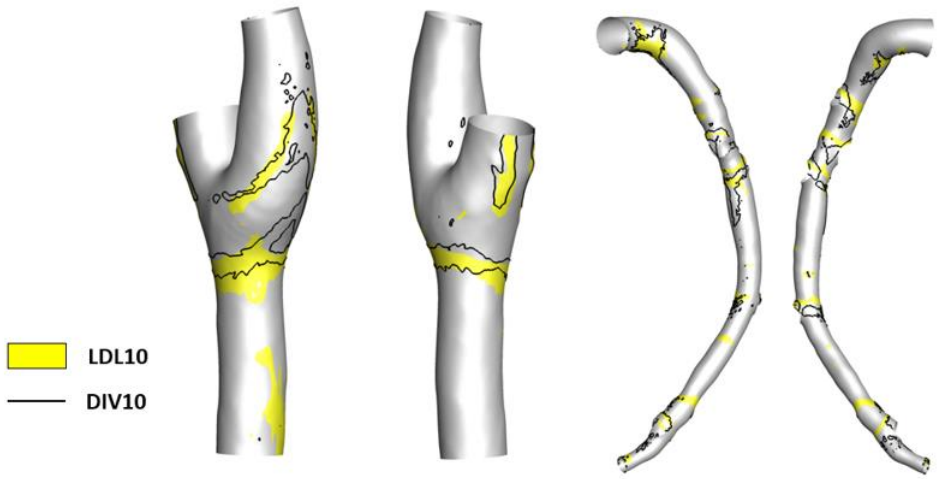

Figure 3.8 Represents the clipped surfaces of the common carotid and the right coronary. Critical LDL high concentration regions (LDL90) are displayed (yellow zones) along with low values of the divergence of the WSS vector field (marked with black lines).

In *figure 3.8* the early mentioned co-localization is more appreciable because of a focus that was made on areas where the values of LDL and DIV are, respectively, higher and lower than the thresholds proposed in section 2.2.5.3 (LDL90 and DIV10). The highest level of co-localization can be evaluated at the external wall of the ECA with an almost

perfect contour made by the DIV10 around the LDL90 surface area.

3.4.2 WSS-based descriptors

To compare the ability of WSS contraction regions as marker of LDL luminal polarization with respect to classical WSS-based descriptors, a specific analysis on the co-localization of those descriptors with LDL polarization regions was conducted.

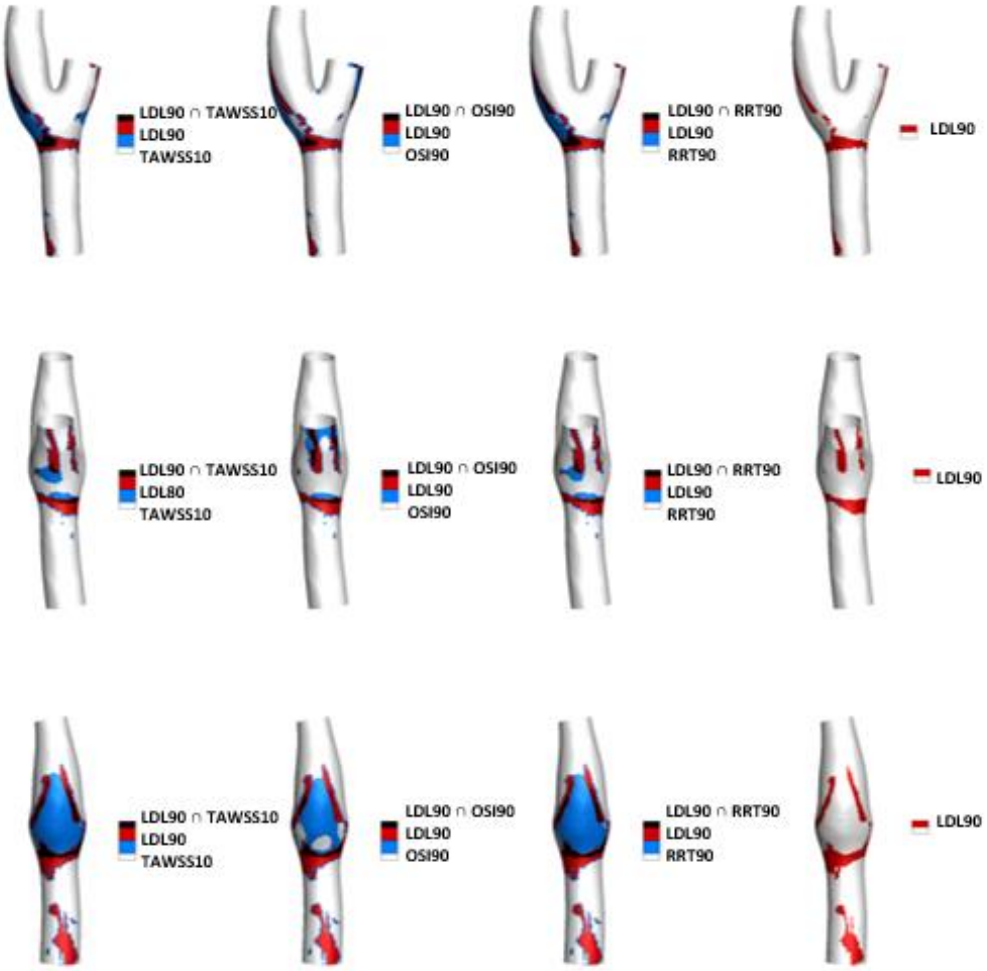

Figure 3.9 A representation of the overlapping between WSS-based descriptors and LDL critical zones on the carotid bifurcation.

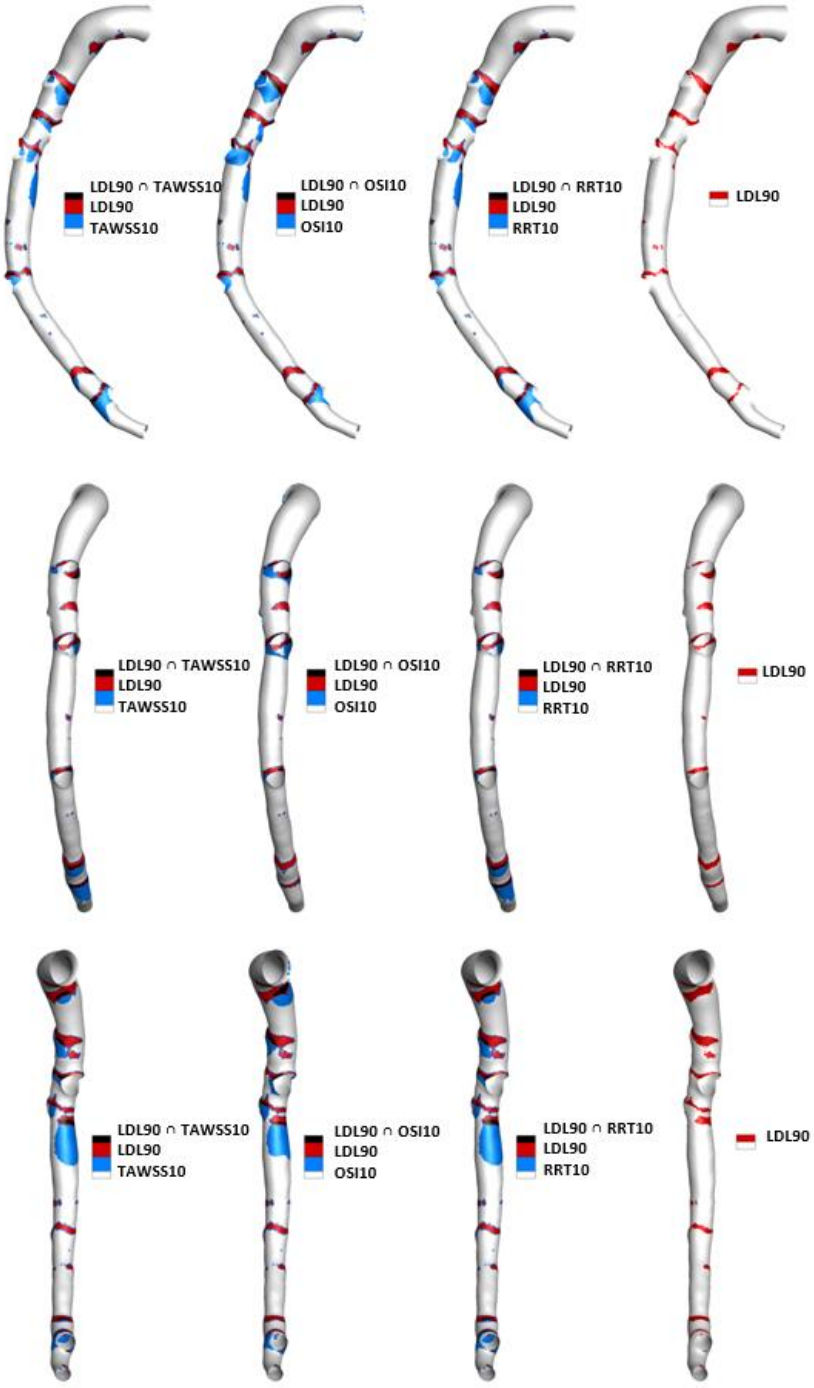

Figure 3.10 A representation of the overlapping between WSS-based descriptors and LDL critical zones on the right coronary artery.

Results of the latter are presented in *Figure 3.9* and *3.10*. In detail, for each descriptor involved in the analysis, luminal surface areas of disturbed flow (i.e., TAWSS10, OSI90, and RRT90) are displayed in blue, LDL90 surface area is reported in red, and their overlap is coloured by black. From a visual inspection of the figures, only a limited co-localization emerged for each descriptor for both models. More in detail, as concerns the carotid bifurcation, TAWSS10, OSI90 and RRT90 are mainly represented by wide areas localized in the carotid bulb while LDL90 is mainly located at the basis of the carotid bifurcation with only two restricted areas along the outer walls of the ICA and the ECA.

As concerns the RCA, a visual inspection points out an apparent co-localization (with the exception of a wide area in the middle of the internal curvature of the vessel) of the early mentioned areas (LDL90, TAWSS10, OSI90 and RRT90). However, WSS-based descriptors areas appear to be wider and slightly shifted with respect to LDL90 areas. This lack of co-localization does not allow an accurate identification of the LDL90 areas along the arterial luminal surfaces.

3.4.3 Similarity analysis

To quantify the qualitative results of the co-localization analysis, the *similarity index* (SI) was computed for each descriptor, weighing the percentage overlap between each of TAWSS10, OSI90, RRT90 and DIV10 and LDL90.

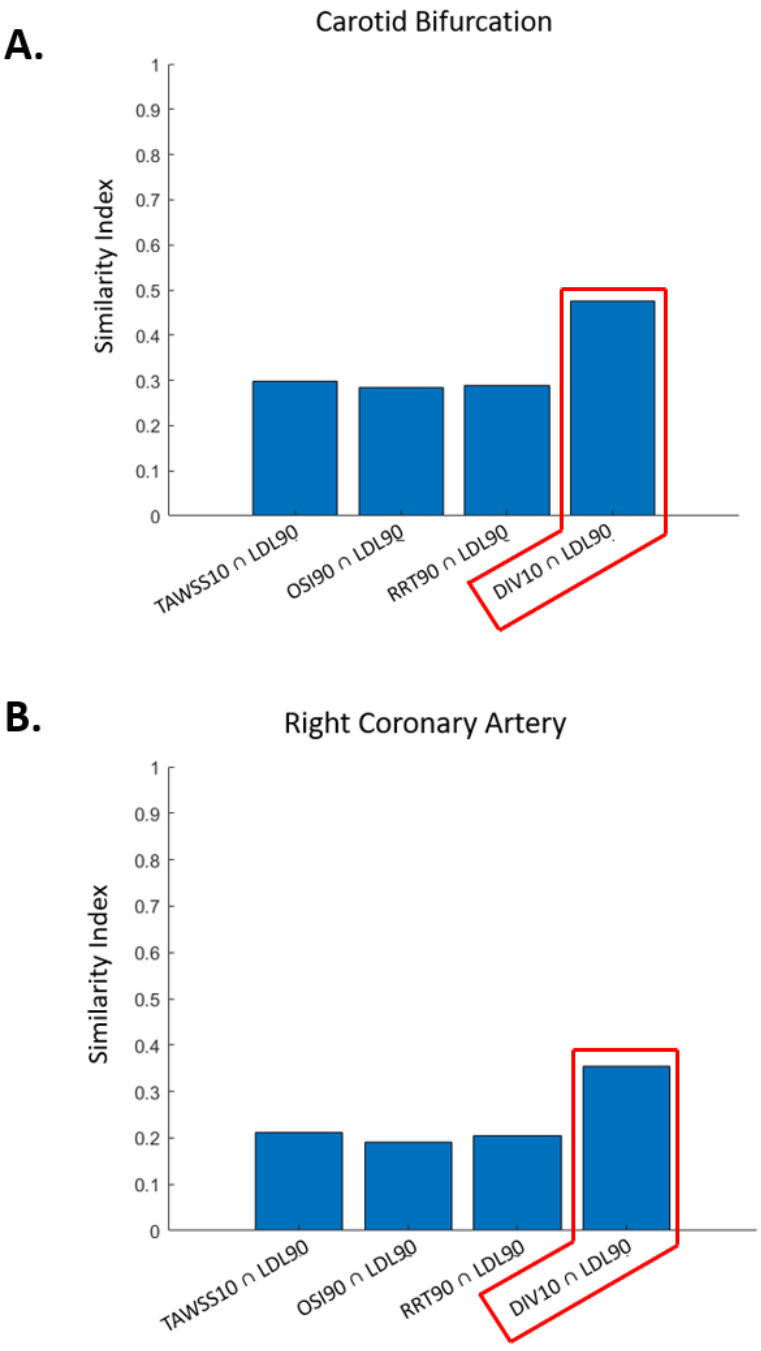

3.11 Similarity Index of the WSS-based descriptors and the divergence of the WSS vector field of the carotid bifurcation (**A**) and of the right coronary artery (**B**).

As represented in *figure 3.11 A* and *B*, divergence of the WSS vector field has a wider overlapped area with LDL polarization regions with respect to other descriptors. In detail, the co-localization of the WSS-based descriptors seems to be at the same level with a SI that goes from a minimum value of 0.19 (LDL90 ∩ OSI90 for the right coronary artery) to a maximum value of 0.29 (LDL90 ∩ TAWSS10 for the carotid bifurcation). The SI of LDL90 ∩ DIV10, indeed, exceed the previous SIs with a value of 0.35 for the right coronary and of 0.47 for the carotid bifurcation. These numbers quantify the accuracy of the WSS contraction regions as marker of luminal LDL polarization.

To better evaluate the predominance of divergence over the other descriptors, the percentage difference of the divergence SI with the SI of TAWSS, OSI and RRT was calculated and reported in *figure 3.12*.

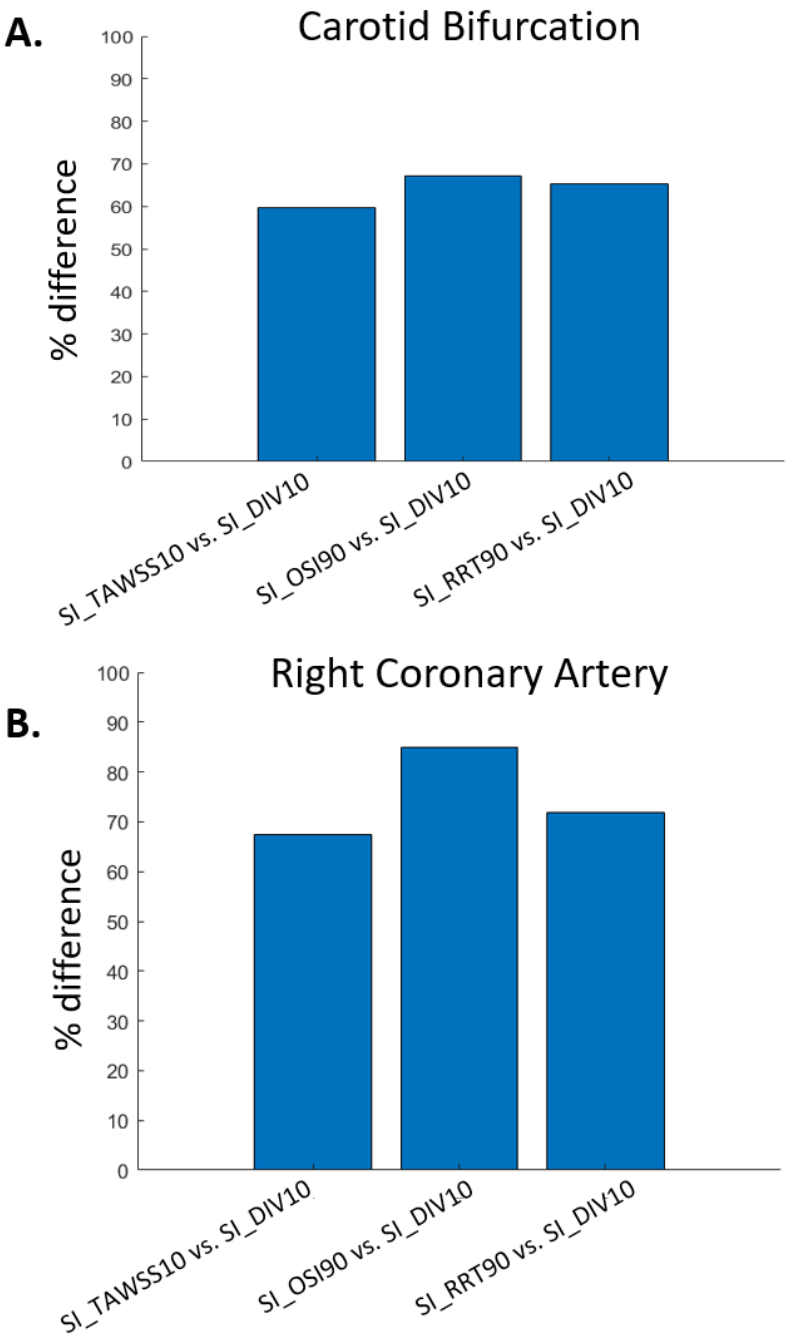

Figure 3.12 A representation of the percentage difference between the similarity index of divergence of WSS vector field with respect to the similarity index of the WSS-based descriptors of the carotid bifurcation (**A**) and of the right coronary artery (**B**).

As displayed in *figure 3.12 A* and *B*, the predominance of the divergence of WSS vector field over the others descriptors is strongly highlighted by a minimum difference of 60% in the *common carotid* and of 70% in the *right coronary.* These values suggest that divergence can be used as a powerful marker of LDL blood-to-wall mass transfer and that his results can be considered more accurate than the classical WSS-based descriptor analysed.

Chapter 4

Discussion and Conclusions

4.1 Discussion

Personalized computational hemodynamic simulations of mass transport/to-wall transfer in human arteries represent a very useful tool in the understanding of blood-to-wall mass transfer mechanisms (e.g. Li et al., 2017, Mpairaktaris et al., 2017, De Nisco et al., 2018). The low-density lipoproteins transport and transfer were here analysed in order to predict the insurgence of atherosclerosis. However, to analyse a complex real problem in a computational way, there is the need to make some simplifying assumptions which result in a source of uncertainty that must be considered in the interpretation of the results (Roache, 1997). To properly

study and analyse the initiation/progression of the atherosclerotic disease the attention was focused on the exposure of the arterial luminal surface to the so called “disturbed” flow (identified by low and oscillatory WSS values). However, paying attention to recent studies which highlight the weak ability of low/oscillatory WSS to predict plaque localization, a recently proposed Eulerian-based method to analyse the WSS topological skeleton, composed by WSS fixed points connected by WSS manifolds, was considered (Mazzi et al., 2020). The WSS manifolds and fixed points were compared to the LDL polarization to evaluate the WSS topological skeleton as an accurate marker. Briefly, two unsteady-state simulations were run on to reconstructed models of the carotid bifurcation and of the right coronary artery. Appropriate boundary and initial conditions were set to properly simulate fluid motion and blood-to-wall LDL transfer and results were used to represent the LDL polarization on the arterial luminal surfaces, as well as the WSS-based descriptors distribution (TAWSS, OSI and RRT) and the WSS topological skeleton (normalized divergence of the WSS vector field). Moreover, luminal surfaces exposed to

deranged hemodynamics were identified by objective thresholds, one for each descriptor, and each critical area was compared to the LDL polarization. The ability of each descriptor to identify local LDL uptake was quantified through the similarity index (SI). Results of this study were analysed in terms of luminal surface areas exposed to high LDL uptake and co-localization between WSS contraction regions/atherogenic WSS patterns and LDL polarization. These results show that high LDL concentration along the luminal surface appears to be located in luminal regions where the flow is known to be "*disturbed*" due to the non-regular geometry of the vessels (i.e. the carotid sinus, at the basis of the carotid bifurcation as well as the internal side of a curvature, usually responsible for the genesis of sites of recirculation and reattachment of the blood flow). The same result is highlighted by the distribution of the negative values of the divergence of the WSS vector field (contraction regions), mainly located in districts characterized by a non-regular geometry. As concerns the WSS-based descriptors, the imposed thresholds had identified atheroprone surface areas which seems to co-localize with the early mentioned

ones (characterized by deranged hemodynamics) but appear to be wider and slightly shifted. This main difference points out the lack of accuracy that characterize the WSS-based descriptors as weak marker for the LDL uptake identification. Conversely, the strong co-localization between WSS contraction regions and LDL high concentration regions, displayed and quantified in *figures 3.7*, *3.8*, *3.11* and *3.12* by graphical evaluation and by relatively high values of SI, highlight the ability of the WSS topological skeleton to provide an accurate template of the LDL polarization on the arterial luminal surface.

4.2 Conclusions

In conclusion, the results from this study suggest that the recently proposed Eulerian-based method to identify WSS topological skeleton provides an effective template of the LDL blood-to-wall transfer, with e reduction both of computational costs and methodological complexity of classical techniques.

In detail, WSS contraction regions markedly co-localize with LDL luminal polarization and better than classical WSS-based

descriptors of deranged hemodynamics (i.e., TAWSS, OSI, RRT). The latter suggests that: (a) WSS contraction regions may promote near-wall mass transfer; (b) WSS contraction region could be used as surrogate marker of near-wall mass transfer. All those evidences underline that the WSS topological skeleton analysis may contribute to a deeper understanding of the hemodynamics-driven processes for atherosclerosis, thus stimulating further investigations on its impact on vascular pathophysiology.

References

Akram M. Shaaban, Duerinckx André J., 2000. *Wall Shear Stress and Early Atherosclerosis*. American Journal of Roentgenology 174, 1657-1665.

Amir Ravandi, Kuksis A., Shaikh Nisar A. , 2000. *Glucosylated Glycerophosphoethanolamines are the Major LDL Glycation Products and Increase LDL Susceptibility to Oxidation. Evidence of Their Presence in Atherosclerotic Lesions*, in Arteriosclerosis, Thrombosis, and Vascular Biology 20, 467-477.

Arzani A., Shadden Shawn C., 2018. *Wall shear stress fixed points in cardiovascular fluid mechanics*. Journal of Biomechanics 73, 145-152.

Warboys Christina M., Amini Narges, De Luca Amalia, Evans Paul C. , 2011. *The role of blood flow in determining the sites of atherosclerotic plaques*. F1000 Medicine Report, 3:5.

De Nisco G., Hoogendoorn A., Chiastra C., Gallo D., Kok A.M., Morbiducci U., Wentzel J.J., 2020a. *The impact of helical flow on coronary atherosclerotic plaque development.* Atherosclerosis 116, 1136-1146.

De Nisco G., Kok A.M., Chiastra C., Gallo D., Hoogendoorn A., Migliavacca F., Wentzel J.J., Morbiducci U., 2019. *The Atheroprotective Nature of Helical Flow in Coronary Arteries.* Ann Biomed Eng 47, 425-438.

De Nisco G., Tasso P., Calò K., et al., 2020b. *Deciphering ascending thoracic aortic aneurysm hemodynamics in relation to biomechanical properties*. Medical Engineering & Physics 82, 119-129.

De Nisco G., Zang P., Calò K., Liu X., Ponzini R., Bignardi C., Rizzo G., Deng X., Gallo D., Morbiducci U., 2018. *What is needed to make low-density lipoprotein transport in human aorta computational models suitable to explore links to atherosclerosis? Impact of initial and inflow boundary conditions*. Journal of Biomechanics 68, 33-42.

Gallo D., Bijari P. B., Morbiducci U., Qiao Y., Xie Y. J., Etesami M., Habets D., Lakatta E.G., Wasserman B.A., Steinman D. A., 2018. *Segment-specific associations between local haemodynamic and imaging markers of early atherosclerosis at the carotid artery: an in vivo human study*. Journal of the Royal Society Interface 15(147):20180352.

Gallo D., DeSantis, G., Negri, F., Tresoldi, D., Ponzini, R., Massai, D., Deriu, M.A., Segers P., Verhegghe B.,

Rizzo, G., Morbiducci, U., 2012. *On the Use of in vivo measured flow rates as boundary conditions for image-based hemodynamic models of the human aorta. Implications for indicators of abnormal flow.* Annals of Biomedical Engineering 40, 729-741.

Gallo D., Steinman D. A., Morbiducci U., 2016. *Insights into the co-localization of magnitude-based versus direction-based indicators of disturbed shear at the carotid bifurcation*. Journal of Biomechanics 49(12), 2413-9.

He, X., Ku, D.N., 1996. *Pulsatile flow in the human left coronary artery bifurcation: average conditions*. ASME Journal of Biomechanics Engineering 118(1),74-82.

Himburg, H.A., Grzybowski D.M., Hazel, A.L., La Mack J.A., Li X.M., Friedman M.H., 2004. *Spatial comparison between wall shear stress measures and porcine arterial endothelial permeability.* American Journal of Physiology Heart and Circulatory Physiology 286, H1916–H1922.

Hoogendoorn A, Kok AM, Hartman EMJ, De Nisco G., Casadonte L., Chiastra C., Coenen A., Korteland S..A, Van der Heiden K., Gijsen F.J.H., Duncker D.J., van der Steen A.F.W., Wentzel J.J., 2020.

Multidirectional wall shear stress promotes advanced coronary plaque development: comparing five shear stress metrics. Cardiovasc Res 116(6), 1136-1146.

Ku D.N., Giddens D.P., Zarins C.K., Glagov S., 1985. *Pulsatile flow and atherosclerosis in the human carotid bifurcation. Positive correlation between plaque location and low and oscillating shear stress.* Arteriosclerosis 5, 293-302.

Kwak Brenda R., Bäck M., Bochaton-Piallat M., Caligiuri G., Daemen Mat J.A.P., Davies Peter F., Hoefer Imo E., Holvoet P., Hanjoong Jo, Krams R., Lehoux S., Monaco C., Steffens S., Virmani R., Weber C., Wentzel J.J., Evans P.C., 2014. *Biomechanical factors in atherosclerosis: mechanisms and clinical implications*. European Heart Journal 35(43), 3013-20.

Lever M.J., Jay M.T., Coleman P.J., 1996. *Plasma protein entry and retention in the vascular wall: possible factors in atherogenesis.* Can. J. Physiol. Pharmacol. 74, 818-23

Li X., Liu X., Zhang P., Feng C., Sun A., Kang H., Deng X., Fan Y., 2017. *Numerical simulation of haemodynamics and low-density lipoprotein transport in the rabbit*

aorta and their correlation with atherosclerotic plaque thickness. Journal of the Royal Society Interface 14(129), 20170140.

Malek A.M., Alper S.L., Izumo, S., 1999. *Hemodynamic shear stress and its role in atherosclerosis.* JAMA 282, 2035-2042.

Mazzi V., Gallo D., Calò K., Najafi M., Khan M.O. et al. 2020, *A Eulerian method to analyse wall shear stress fixed points and manifolds in cardiovascular flows*, Biomech Model Mechanobiol. 19(5), 1403-1423.

Morbiducci U., Kok A. M.; Kwak B.R.; Stone P.H.; Steinman D.A.; Wentzel J.J., 2016. *Atherosclerosis at arterial bifurcations: evidence for the role of haemodynamics and geometry*. Thromb Haemost 115(3), 484-92.

Morbiducci, U., Mazzi, V., Domanin, M. et al., 2020. *Wall Shear Stress Topological Skeleton Independently Predicts Long-Term Restenosis After Carotid Bifurcation Endarterectomy*. Ann Biomed Eng., https://doi.org/10.1007/s10439-020-02607-9.

Mpairaktaris D.G., Soulis J.V., Giannoglu G.D., 2017. *Low density lipoprotein transport though patient-*

specific thoracic arterial wall. Computers in Biology and Medicine 89, 115-126.

Nielsen L.B., 1996. *Transfer of low-density lipoprotein into the arterial wall and risk of atherosclerosis.* Atherosclerosis 123, 1-15.

Patel C.Y., Eggen D.A., Strong J.P., 1980. *Obesity, smoking and atherosclerosis: A study of interassociations*. Atherosclerosis 36, 481-490.

Peiffer V., Sherwin S.J., Weinberg P.D., 2013. *Does low and oscillatory wall shear stress correlate spatially with early atherosclerosis? A systematic review*. Cardiovasc Res 99(2), 242-50.

Peter F.D., Shi C., DePaola N., Helmke B.P., Polacek D.C., 2008. *Hemodynamics and the Focal Origin of Atherosclerosis. A Spatial Approach to Endothelial Structure, Gene Expression, and Function*. Annals of the New York Academy of Science 947, 7-16.

Pinto S.I.S., Campos B.L.M., 2016. *Numerical study of wall shear stress-based descriptors in the human left coronary artery.* Computer methods in

Biomechanics and Biomedical Engineering 19(13), 1443-55.

Roache P.J., 1997. Quantification of uncertainty in Computational Fluid Dynamics. Annual Review of Fluid Mechanics 29, 123-160.

Schneck D.J., 1995. *An outline of cardiovascular structure and function*, in The biomedical engineering handbook. Ed. Bronzino, CRC PressInc., Hartford (CT), USA.

Steinman D.A., Thomas J.B., Ladak H.M., Milner J.S., Rutt B.K., Spence J.D., 2002. *Reconstruction of carotid bifurcation hemodynamics and wall thickness using computational fluid dynamics and MRI*. Magn Reson Med 47(1), 149-59.

Stocker R., Keaney J.F., 2004. *Role of Oxidative Modifications in Atherosclerosis*. Physiological Reviews 84(4), 1381-478.

Swirski K. Filip , Nahrendorf M., 2013. *Leukocyte Behavior in Atherosclerosis, Myocardial Infarction, and Heart Failure*. Science 339(6116), 161-6.

Tada, S., 2010. *Numerical study of oxygen transport in a carotid bifurcation.* Physics in Medicine and Biology 55, 3993-4010.

Tarbell J.M., 2003. *Mass transport in arteries and the localization of atherosclerosis*. Annual Review of Biomedical Engineering 5, 79-118.

van der Giessen AG, Groen HC, Doriot P-A, de Feyter PJ, van der Steen AFW, van de Vosse FN, et al., 2011. *The influence of boundary conditions on wall shear stress distribution in patients specific coronary trees*. J Biomech 44, 1089-1095.

Wada, S., Karino, T., 2002. *The theoretical prediction of low-density lipoproteins concentration at the luminal surface of an artery with a multiple bend.* Annals of Biomedical Engineering 30, 778-791.

W Shi , Haberland M.E., Jien M.L., Shih D.M., Lusis A.J., 2000. *Endothelial responses to oxidized lipoproteins determine genetic susceptibility to atherosclerosis in mice*. Circulation 102(1), 75-81.